ACS NANO

NOVEMBER 12, 2024 VOLUME 18 NUMBER 45

pubs.acs.org/acsnano

Defining nanoscience and nanotechnology

ACS Publications
Most Trusted. Most Cited. Most Read.

www.acs.org

ACS NANO

Open Access

www.acsnano.org

ARTICLE

Atomically Sharp 1D Interfaces in 2D Lateral Heterostructures of VSe_2—$NbSe_2$ Monolayers

Xin Huang, Héctor González-Herrero, Orlando J. Silveira, Shawulienu Kezilebieke, Peter Liljeroth, and Jani Sainio*

Cite This: *ACS Nano* 2024, 18, 31300–31308

Read Online

ACCESS | Metrics & More | Article Recommendations | Supporting Information

ABSTRACT: **van der Waals heterostructures have emerged as an ideal platform for creating engineered artificial electronic states. While vertical heterostructures have been extensively studied, realizing high-quality lateral heterostructures with atomically sharp interfaces remains a major experimental challenge. Here, we advance a one-pot two-step molecular beam lateral epitaxy approach and successfully synthesize atomically well-defined 1T-VSe_2—1H-$NbSe_2$ lateral heterostructures. We demonstrate the formation of defect-free lateral heterostructures and characterize their electronic structure by using scanning tunneling microscopy and spectroscopy together with density functional theory calculations. We find additional electronic states at the 1D interface as well as signatures of Kondo resonances in a side-coupled geometry. Our experiments explored the full potential of lateral heterostructures for realizing exotic electronic states in low-dimensional systems for further studies of artificial designer quantum materials.**

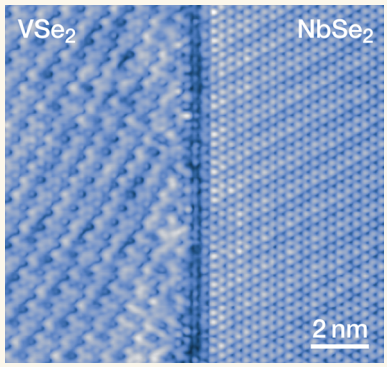

KEYWORDS: *TMDC, lateral heterostructure, STM, DFT, MBE*

Heterostructures of two-dimensional (2D) materials are seen as one of the most flexible platforms to study correlated electronic states and realize intricate phenomena in condensed matter systems.[1−3] Most van der Waals (vdW) heterostructures are assembled through vertical stacking, where layers interact only via van der Waals forces. These vertical heterostructures de facto realize an effective 2D system. In addition to these 2D systems, it would be desirable to have access to one-dimensional (1D) structures, where different electronic phenomena can arise. 1D lattices with a lower dimensional structure also provide a simpler prototype to understand many-body physics. However, dimensionality reduction starting from a higher dimension remains challenging; it is inherently difficult to fabricate 1D structures with top-down methods, e.g., mechanical exfoliation and transfer. Currently, almost all experimentally realized 1D structures in 2D materials are naturally occurring, for example, grain boundaries or domain walls.[4−7]

On the other hand, fabricating lateral heterostructures by bottom-up synthesis offers intriguing possibilities for creating 1D structures. Compared to their vertical counterparts, lateral heterostructures or in-plane heterojunctions have covalent bonds between the components and can form artificial 1D structures capable of hosting exotic electronic states. However, the most common method to produce lateral heterostructures—chemical vapor deposition (CVD)—has considerable drawbacks: the atomic-scale structure of CVD-grown interfaces typically suffers from a high density of imperfections, such as elemental doping and alloying, various defects, and dislocations.[8−19] In addition, most attention on lateral heterostructures in transition metal dichalcogenides (TMDCs) to date has focused on homophase semiconductor-semiconductor junctions (e.g., MoS_2, $MoSe_2$, WS_2, and WSe_2), where the two components have the same crystal structure, e.g., 1H- with 1H-phase.[8−16,20,21]

In this work, we choose two heterophase metallic TMDC monolayers, vanadium diselenide (VSe_2) and niobium diselenide ($NbSe_2$), with different crystal phases of 1T and 1H with both having electronic structures where electron correlations play a significant role. VSe_2 is metallic in its monolayer octahedral 1T structure, and it has been reported to have various possible magnetic ground states competing with charge density wave (CDW) order depending on factors such as defect density, doping, and strain.[22−30] The other ingredient, 1H-phase of $NbSe_2$, is a 2D metal exhibiting significant electron correlations, and CDW and superconduct-

Received: July 30, 2024
Revised: October 16, 2024
Accepted: October 24, 2024
Published: November 2, 2024

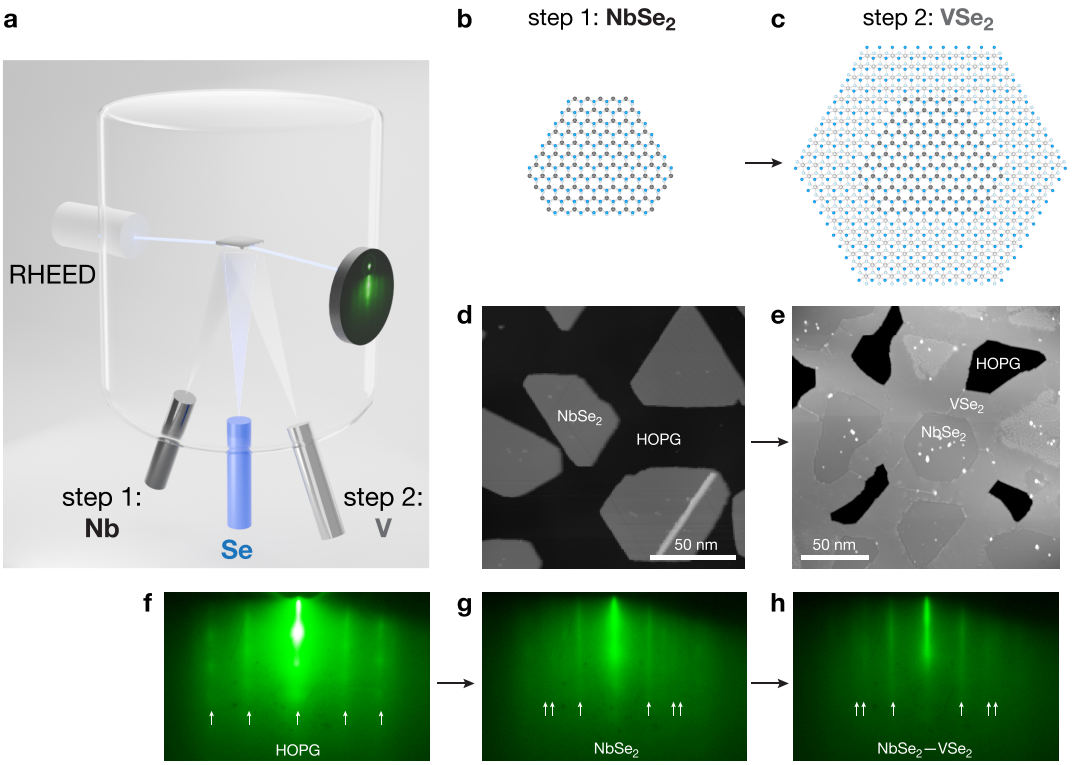

Figure 1. Synthesis of the lateral heterostructures. (a) Illustration of our one-pot, two-step lateral epitaxy. (b) Schematic of a $NbSe_2$ island and (c) in-registry lateral epitaxy of VSe_2 surrounding the $NbSe_2$ island. (d) Scanning tunneling microscopy (STM) topography image of the sample after step 1: growth of $NbSe_2$. V_s = +1 V, I_t = 2 pA. (e) STM image after step 2: growth of VSe_2. V_s = −1.5 V, I_t = 10 pA. (f–h) Reflection high-energy electron diffraction (RHEED) patterns of the substrate HOPG (f), monolayer $NbSe_2$ islands (step 1, g), and VSe_2—$NbSe_2$ lateral heterostructures (step 2, h).

ing orders at low temperatures (superconducting $T_c \sim 1$ K for a monolayer).[31−37]

Here, we demonstrate a one-pot, two-step lateral epitaxy technique to fabricate atomically sharp and well-defined lateral heterostructures of 1T-VSe_2—1H-$NbSe_2$ by molecular beam epitaxy (MBE). We probe them by low-temperature scanning tunneling microscopy (STM) and spectroscopy (STS) and identify two different 1D interface structures corroborated by density functional theory (DFT) calculations. These heterostructures exhibit 1D interfacial states and signatures of Kondo resonances in an atomic-scale side-coupled geometry. This work demonstrates an approach for achieving complex lateral heterostructures with atomically well-defined 1D interfaces where it is possible to realize correlated many-body states via lateral coupling.

RESULTS AND DISCUSSION

Synthesis and Structure of the Lateral Heterostructures. We overcome the challenges in CVD[8−16,20] by introducing a one-pot two-step lateral epitaxy method utilizing MBE (Figure 1 and Methods). The first step is to grow monolayer islands of 1H-phase $NbSe_2$ at 550 °C with well-defined and straight edges (Figure 1b,d). The second step is the lateral epitaxy growth of 1T-VSe_2 at 375 °C (Figure 1c,e and Supplementary Figures S1 and S2), using the 1H-$NbSe_2$ islands' edges as seeds.[38,39] Growth temperature and growth sequence play a crucial role[40] in lateral epitaxy: the material with higher growth temperature should be synthesized first in order to preserve island morphology and the edge structure and to prevent unwanted alloying in the next steps. Our molecular beam lateral epitaxy growth can be monitored in situ via reflection high-energy electron diffraction (RHEED). During step 1, the RHEED pattern gradually develops stripes of $NbSe_2$ in addition to the pattern related to the highly oriented pyrolytic graphite (HOPG) substrate (Figure 1f,g). Subsequently, during step 2, the RHEED pattern of the newly formed lateral heterostructure basically overlaps with the one of the $NbSe_2$, because the nominal lattice constant of VSe_2 is very similar to that of $NbSe_2$ (~0.1 Å difference) and the overall increasing coverage of the monolayer leads to dimming and the eventual disappearance of the HOPG RHEED pattern (Figure 1h). We have also calculated the lattice constants from RHEED: for 1T-VSe_2, we obtained 3.36 ± 0.09 Å (Supplementary Figure S3), for 1H-$NbSe_2$ 3.46 ± 0.09 Å, and for the $NbSe_2$−VSe_2 heterostructure 3.38 ± 0.09 Å.

We confirm the growth of 1H-$NbSe_2$ and 1T-VSe_2 by their STM topography images with typical charge density waves [3 × 3 for 1H-$NbSe_2$,[31] $\sqrt{3} \times 2$ and $\sqrt{3} \times \sqrt{7}$ for 1T-VSe_2[23,29,41] (see Supplementary Figures S2, S5 and S6)]. Creating lateral heterostructures from such systems provides opportunities for research on 2D charge density wave orders. In our heterostructures, the intrinsic CDWs of both materials extend right up to the interface (Figure 2 and Supplementary Figures S5−S10), where they abruptly switch from the characteristic CDW of 1H-$NbSe_2$ to that of 1T-VSe_2 in contrast to a similar system showing a CDW proximity effect.[37] The undeformed CDWs indicate that there is no observable in-plane lattice distortion, implying a lack of significant amounts of, e.g., strain or doping being induced at the interface, as especially the CDW in 1T-VSe_2 should be sensitive to those.[26]

We find two different types of lateral heterostructures, as shown in Figure 2. The 1D interfaces are atomically sharp

https://doi.org/10.1021/acsnano.4c10302
ACS Nano 2024, 18, 31300−31308

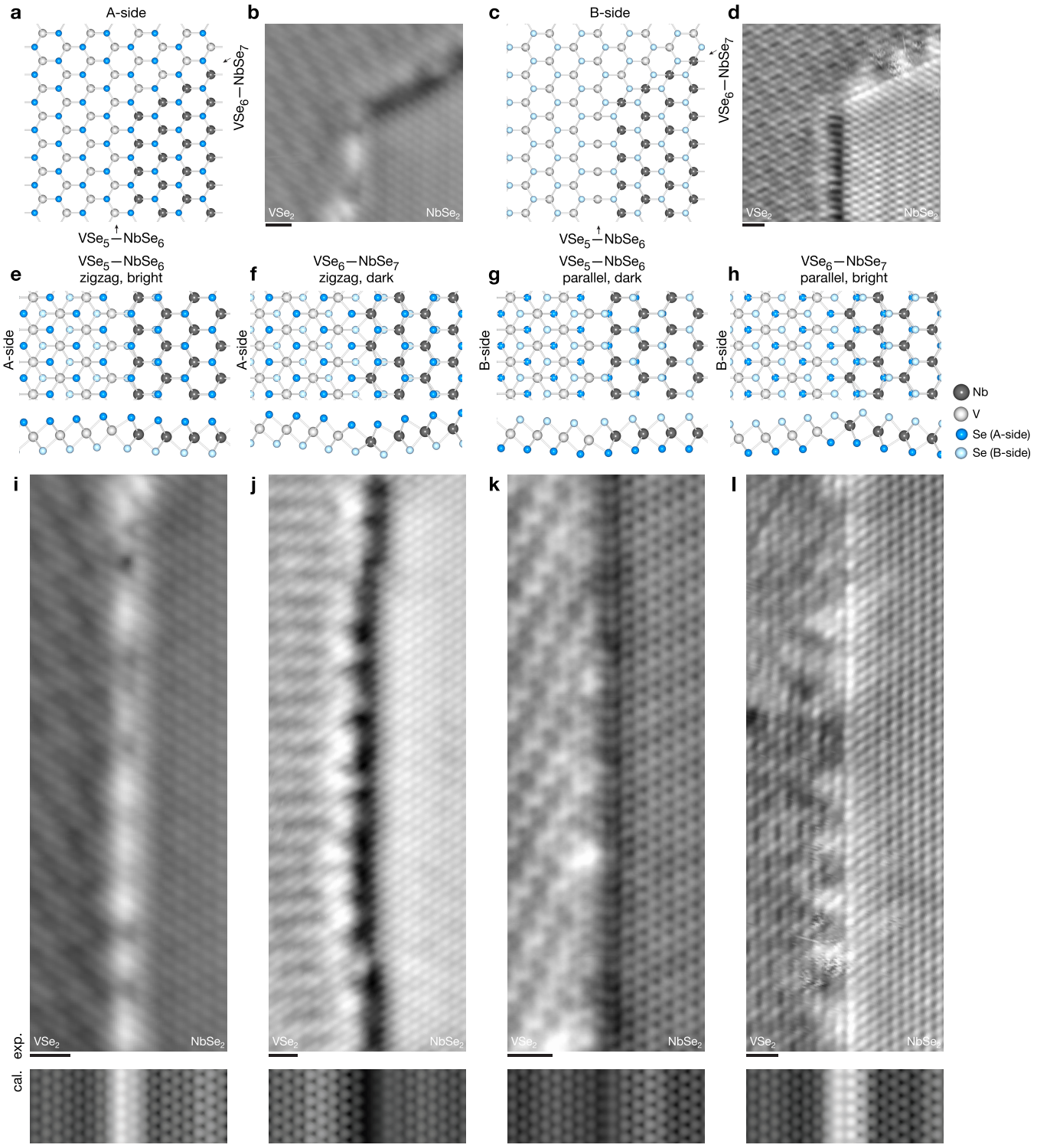

Figure 2. Two types of lateral heterostructures. (a) A-side view (with A-side Se atoms only) and (b) its STM topography image. (c) B-side view (with B-side Se atoms only) and (d) its STM topography image. (e–h) Top and side view of the two types of lateral heterostructures and (i–l) their corresponding atomically resolved STM topography images (experimental and calculated). Scan parameters: (b, d, i, j, l) V_s = −1 V, I_t = 100 pA. (k) V_s = −0.99 V, I_t = 50 pA. Calculated STM images, V_s=−0.5 V. All scale bars are 1 nm.

without cross-contamination, doping, or alloying, with the length of the straight sections extending up to ∼20 to 40 nm (Figure 2 and Supplementary Figures S6–S9), which to our knowledge are the longest high-quality TMDC lateral heterostructures grown so far.[19] The first-grown 1H-$NbSe_2$ islands mostly have a hexagonal shape with 120° corners. Considering the crystal structure, this means that the neighboring edges are crystallographically distinct, i.e., with alternating edge terminations with e.g., Nb- or Se-terminated edges.[42,43] The subsequent epitaxy of 1T-VSe_2 will most likely form Nb–Se–V chemical bonds over the interface, especially in a Se-rich growth environment. Combining this with the 1T-VSe_2 crystal structure, we can identify four different types of possible lateral heterostructures, with vanadium and niobium

https://doi.org/10.1021/acsnano.4c10302
ACS Nano 2024, 18, 31300–31308

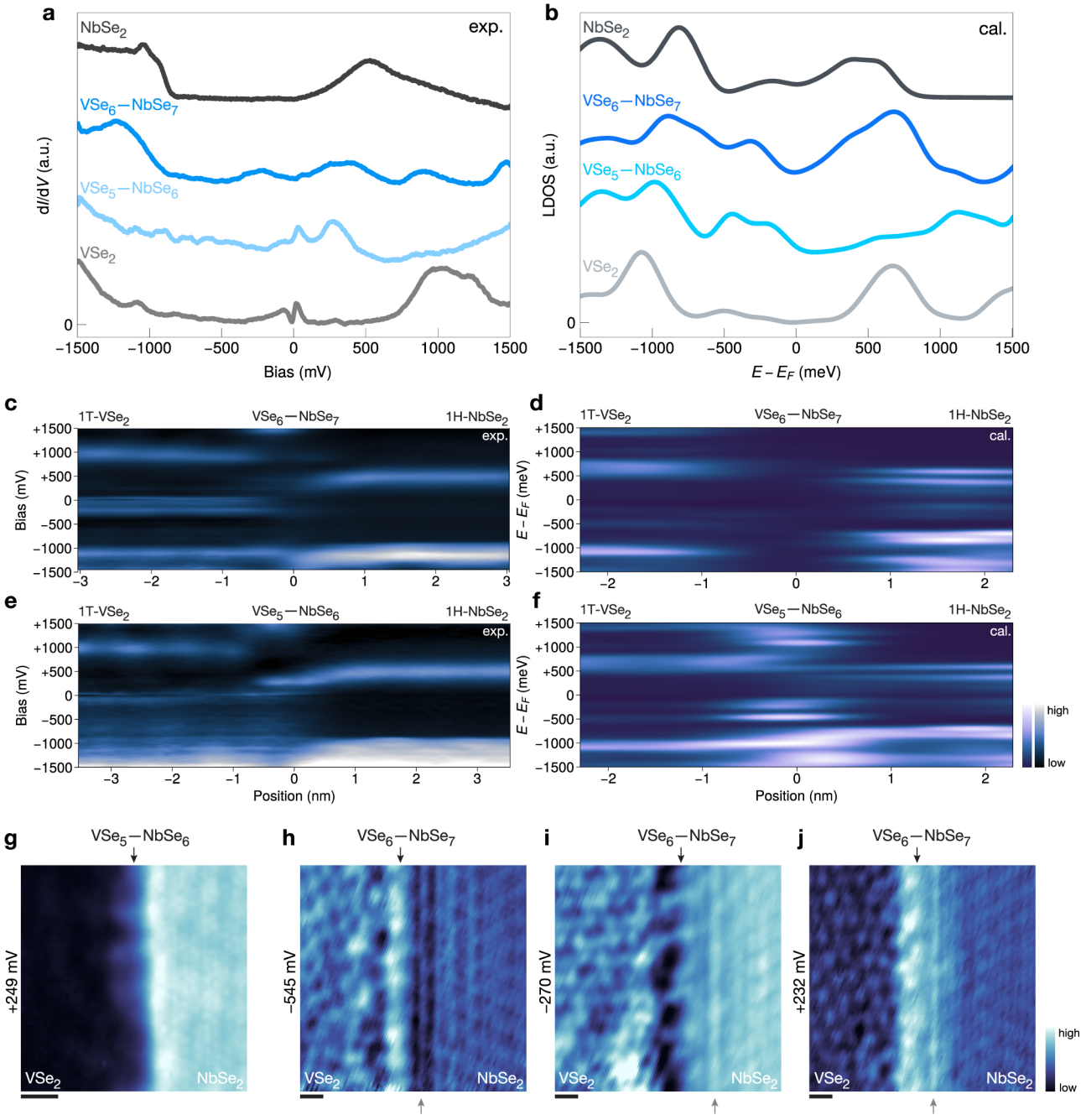

Figure 3. Electronic structure of the lateral heterostructures. (a) dI/dV spectra of 1H-$NbSe_2$, 1T-$VSe2_2$, VSe_5—$NbSe_6$, and VSe_6—$NbSe_7$ interfaces (shifted vertically for clarity). (b) DFT-calculated LDOS of 1H-$NbSe_2$, 1T-$VSe2_2$, VSe_5—$NbSe_6$, and VSe_6—$NbSe_7$ interfaces (shifted vertically for clarity). (c–f) Experimental dI/dV spectra and calculated LDOS along a line across the VSe_6—$NbSe_7$ (panels c and d) and VSe_5—$NbSe_6$ (panels e and f) interfaces. (g) dI/dV map of the 1D interfacial state of VSe_5—$NbSe_6$, at +249 mV (V_{mod} = 4 mV). (h–j) Constant-current dI/dV maps of VSe_6—$NbSe_7$ interface at −545, −270, and +232 mV, respectively (V_{mod} = 10 mV), which show additional line−like LDOS modulation inside 1H-$NbSe_2$ in the vicinity of the VSe_6—$NbSe_7$ interface. Top black arrows indicate the interfaces, while bottom gray arrows mark the modulation features. All scale bars are 1 nm.

coordination numbers between 5 and 7 (Supplementary Figures S16 and S18). Corroborated by our DFT calculations, we identify the two most stable heterostructures, and we label them as VSe_5—$NbSe_6$ and VSe_6—$NbSe_7$ (Figure 2a,c). Also, other types of structures have been considered, but they either fail to produce the correct type of atomic arrangement seen in Figure 2 or are inconsistent with in-registry growth around 120° corners of 1H-$NbSe_2$ islands (Supplementary Figure S16).

However, depending on which side of these structures grows on the substrate (and hence which side faces the STM tip), these two types of lateral heterostructures show four different STM topographies (arising mostly from the top layer of Se atoms), as shown in Figure 2e–h and labeled zigzag or parallel with bright or dark contrast. Hence, the two different interface structures, VSe_5—$NbSe_6$ and VSe_6—$NbSe_7$, can appear in two different orientations on the surface corresponding to different sides of the monolayer, labeled A-side and B-side. If imaged on

https://doi.org/10.1021/acsnano.4c10302
ACS Nano 2024, 18, 31300−31308

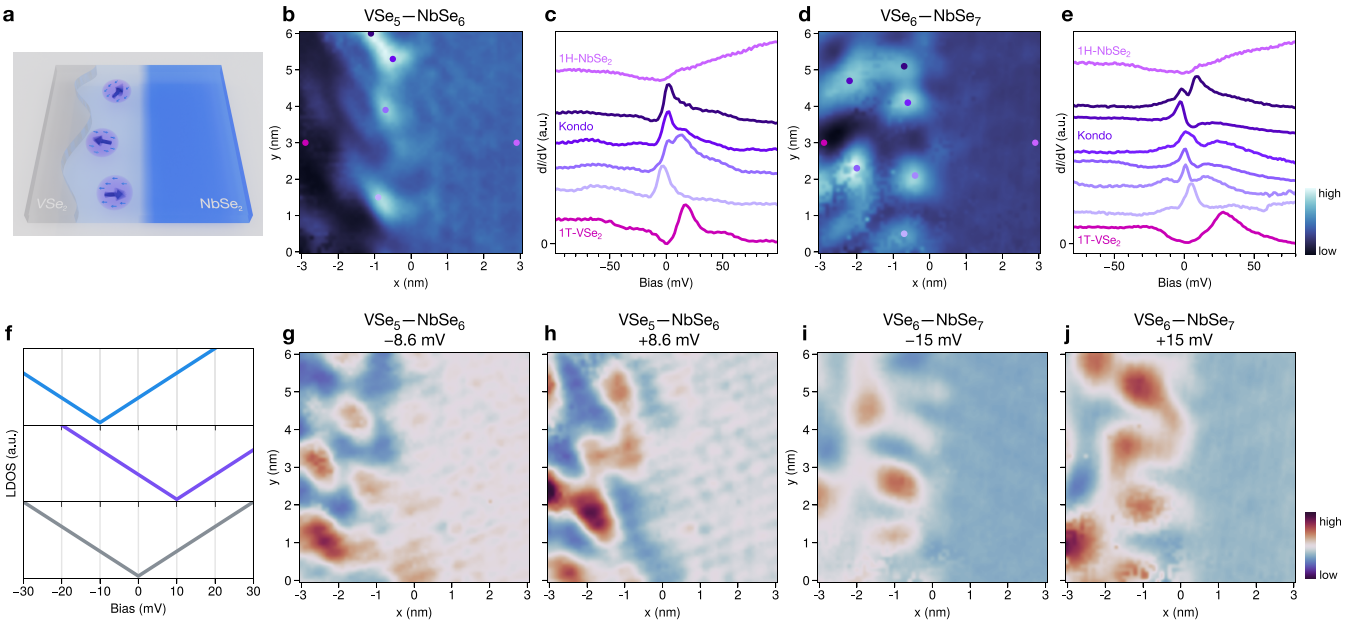

Figure 4. Signatures of the Kondo effect in a side-coupled geometry and contrast inversion near the interfaces. (a) Schematic of Kondo singlets in a side-coupled geometry. Conduction electrons (light blue area) screen localized moments (purple arrows), forming Kondo singlets. (b) dI/dV map at −0.8 mV of VSe_5—$NbSe_6$ interfaces, V_{mod} = 2 mV. (c) Point dI/dV spectra from positions marked in (b) (shifted vertically for clarity). (d) dI/dV map at 0 mV of VSe_6—$NbSe_7$ interfaces, V_{mod} = 1 mV. (e) Point dI/dV spectra from positions marked in (d) (shifted vertically for clarity). (f) Schematic of the V-shaped LDOS around the Fermi level of different spots inside 1T-VSe_2: negatively charged (top), positively charged (middle), and neutral without charge doping (bottom). (g, h) Contrast inversion of a dI/dV map of VSe_5—$NbSe_6$ at ±8.6 mV, V_{mod} = 2 mV. (i, j) Contrast inversion of a dI/dV map of VSe_6—$NbSe_7$ at ±15 mV, V_{mod} = 1 mV.

the A-side, the VSe_5—$NbSe_6$ interface shows a bright zigzag structure and VSe_6—$NbSe_7$ a dark zigzag; if scanning on the B-side, VSe_5—$NbSe_6$ shows a dark parallel structure and VSe_6—$NbSe_7$ a bright parallel one.

Our DFT calculations also give the correct contrast from the top layer Se atoms in simulated STM images compared to the experimental ones (Figure 2i–l). The DFT calculations suggest that the interfaces have a slight structural deformation producing a structure similar to that of the 1T′-phase, and the trend of bright or dark contrast comes in part from a small corrugation at the interface (Figure 2e–h). The contrast also has an electronic component discussed later. We find that the bright and dark contrasts alternate between the adjacent edges of hexagonal 1H-$NbSe_2$ islands (see Figure 2b,d, and Supplementary Figures S6–S9). In addition, interfaces around a single 1H-$NbSe_2$ island are either zigzag or all parallel. These two experimental observations further support the structural assignment above and are consistent with our DFT calculations (Figure 2e–h).

Electronic Structure of the 1D Interfaces. We focus next on the electronic behavior of the two lateral heterostructures on the A-side with zigzag interfaces (Figure 3). The differential conductance (dI/dV) spectrum of monolayer 1H-$NbSe_2$ shows a peak at around +500 mV related to the Nb-based conduction band, and the peak ∼−1100 mV is related to its valence band.[31,44] The conduction band crosses the Fermi level away from the Γ-point, and it is difficult to resolve the bottom of the conduction band.[31] Together with the gap between the bottom of the conduction band and the valence band, this results in a bias region with a low dI/dV signal (from ∼0 mV to ∼− 840 mV). The dI/dV of 1T-VSe_2 is consistent with the results reported in the literature,[24,28,45,46] with the signal close to the Fermi level arising from the vanadium d-states and V-shaped features very close to E_F resulting from the CDW.[24,46]

The two interfaces show quite different features compared with each other and the corresponding 1H-$NbSe_2$ and 1T-VSe_2 bulk monolayers. For the VSe_5—$NbSe_6$ interface, a prominent peak shows up around +250 mV (Figure 3a). From the differential conductance (dI/dV) map taken at this energy (Figure 3g), we can confirm that this state is localized at the interface, with a spatial extent of roughly 1 nm. For VSe_6—$NbSe_7$, no additional states are observed but the Nb-based conduction band shifts to lower energy very close to the interface while the valence band of 1T-VSe_2 remains at the same energy. The evolution of the electronic states can be also visualized by recording spectra along a line across the interface, as shown in Figure 3c,e.

DFT-calculated LDOS spectra (Figure 3b,d,f, and Supplementary Figure S15) show similar behavior. The additional electronic state of VSe_5—$NbSe_6$ is reproduced in the calculated LDOS (with an energy shift which is also seen for the monolayer 1T-VSe_2 states). This state is absent at the VSe_6—$NbSe_7$ interface.

We also calculated the projected density of states (PDOS) on the top layer Se atoms at the VSe_5—$NbSe_6$ interface (see Supplementary Figure S17), since they contribute most to the STM signal. The calculations indicate that the bright contrast at the interface is due not only to the corrugation of the Se atoms but also to changes in the electronic structure. The same is true for the VSe_6—$NbSe_7$ interface (dark contrast), but in that case, the effect of the corrugation appears to be larger.

Finally, we observed additional density of states oscillations parallel to the VSe_6—$NbSe_7$ interface on the 1H-$NbSe_2$ side, in addition to its normal 3 × 3 CDW (Figure 3h–j, the constant-current dI/dV maps). This additional modulation could arise

https://doi.org/10.1021/acsnano.4c10302
ACS Nano 2024, 18, 31300−31308

from interference of incident and elastically scattered CDWs or from Friedel oscillations[43,47,48] and it is absent on the VSe_5—$NbSe_6$ interfaces.

Signatures of Kondo Resonances in a Side-Coupled Geometry at the Interfaces. Lateral heterostructures provide an ideal platform to create 1D interfaces that combine properties of different materials and allow for direct visualization of the created designer quantum state in real space. Our heteroepitaxy protocol ensures atomically sharp interfaces, largely eliminating the undesirable interference from imperfections (e.g., defect states). Here, we give one demonstration of such designer phenomena in our artificial composite materials with side-coupled geometry. In addition to the electronic effects discussed in the previous section, we observe both interfaces exhibiting strong localized zero bias anomalies with typical peak or dip-peak features (Figure 4c,e and Supplementary Figures S11 and S12). At the same time, our STS lacks typical inelastic tunneling features that could be associated with spin-flip or magnon excitations.[49−51] While not conclusively proven by, e.g., temperature and magnetic field dependence, we consider the most likely explanation for these zero bias anomalies to be Kondo resonances arising from coupling between localized magnetic moments in 1T-VSe_2 and conduction electrons in 1H-$NbSe_2$ (Figure 4a). These Kondo resonances are unlikely to arise from the coupling between 1T-VSe_2 and the substrate HOPG, since zero bias anomalies in pristine 1T-VSe_2 are absent in our results (Figure 4c,e and Supplementary Figures S11 and S12) and other reports on the pure monolayer 1T-VSe_2/HOPG system.[24,52] The emergence of free magnetic moments in 1T-VSe_2 could be related to the ground state of the material itself, or to an interfacial effect, with contributions from, e.g., inhomogeneous strain and charge transfer. Similar Kondo resonances have been previously observed close to the edges of 1T-VSe_2 islands on bulk 2H-$NbSe_2$.[28] Thus, it is most likely that 1H-$NbSe_2$ acts as the electron bath/charge reservoir, which couples to the localized magnetic moments inside 1T-VSe_2.[24,28,53,54] These lateral heterostructures realize Kondo resonances in a side-coupled geometry (Figure 4a), which has been previously reported only in mesoscopic side-coupled quantum dot experiments.[55−57]

The maximum intensity of the Kondo signal is found inside 1T-VSe_2 rather than exactly at the interface (Figure 4b,d). They can extend in some cases even up to ∼8 nm away from the interface to the VSe_2 side (see Supplementary Figure S12). Besides the appearance of localized moments in VSe_2, the formation of these Kondo singlets depends on the possible spacial range of screening by the conduction electrons of $NbSe_2$. The positions of Kondo sites show real-space modulation, but they are not directly linked with the periodicity of either the VSe_2 lattice or the CDW in 1T-VSe_2 or 1H-$NbSe_2$ (Figure 4b,d), which could be related to the inhomogeneous charge distribution discussed below. This, taken together with the signature of Kondo resonances, suggests a lack of magnetic order in 1T-VSe_2 around the interfaces.

For 1T-VSe_2 near the interface, we also observe a contrast inversion in differential conductance (dI/dV) maps at small positive and negative bias, at energies inside the V-shaped local density of states (LDOS) (see Figure 4f–j and Supplementary Figure S12). We attribute this phenomenon to a spontaneous inhomogeneous electronic charge redistribution in 1T-VSe_2. Hence, at different positions, the electronic doping shifts the 1T-VSe_2's V-shaped LDOS toward positive/negative energy, as suggested in Figure 4f. When obtaining dI/dV maps, e.g., at positive bias +10 mV, the negatively charged spots get brighter contrast, while positively charged spots get darker contrast; and when taking at opposite bias, the contrast of dI/dV maps reverses.[58,59] In comparison, 1H-$NbSe_2$ is basically free from contrast inversion. We speculate that this spontaneous charge redistribution may be a feature of 1T-VSe_2 itself, or a result of charge transfer to/from 1H-$NbSe_2$, which would depend on the CDW periodicity of both 1H-$NbSe_2$ and 1T-VSe_2, and thus could be quite inhomogeneous.

CONCLUSIONS

In this work, we introduce a one-pot, two-step heteroepitaxy method for constructing atomically sharp 1T-VSe_2—1H-$NbSe_2$ lateral heterostructures. We systematically study these defect-free, straight 1D interfaces to reveal their atomic-level geometric and electronic structures using STM and STS experiments corroborated by DFT calculations. We identify two structures, VSe_5—$NbSe_6$ and VSe_6—$NbSe_7$, and find electronic states and charge modulation localized at or near the 1D interfaces. We demonstrate that these types of lateral heterostructures can be used to realize exotic electronic states, in our case Kondo resonances, arising from the coupling of the magnetic moments of 1T-VSe_2 with 1H-$NbSe_2$ conduction electrons. Our work presents a general method for constructing atomically perfect 1D interfaces in TMDC lateral heterostructures for further studies of correlated 1D systems.

METHODS

Synthesis of Heterostructures. We use an enhanced MBE protocol (one-pot two-step molecular beam lateral epitaxy) to synthesize VSe_2, $NbSe_2$, and their lateral heterostructures in ultrahigh vacuum (UHV) (base pressure of ∼8×10^{-9} mbar). Vanadium rod (99.8%, Goodfellow Cambridge Ltd.) and niobium rod (99.9%, MaTecK GmbH) were evaporated by electron-beam heating (EFM 3T, Focus GmbH). Se powder (99.99%, Sigma-Aldrich) was evaporated in an effusion cell at ∼140 °C with a thermal cracker at ∼1200 °C (Thermal cracker cell, MBE-Komponenten GmbH). All samples were grown on highly oriented pyrolytic graphite (HOPG) (ZYB grade, TipsNano Co.), which were previously degassed above ∼600 °C. The VSe_2—$NbSe_2$ lateral heterostructure was synthesized in two steps: first, growing $NbSe_2$ at ∼550 °C with a growth rate of 29 min per monolayer, with 30 min post annealing at ∼400 °C; second, growing VSe_2 at a substrate temperature of ∼375 °C with a growth rate of 14 min per monolayer, with 5 min post annealing at ∼375 °C. Later, to protect materials during transferring to STM, samples were capped in Se vapor with an amorphous Se layer (>10 nm).

STM Measurements. The STM experiments were carried out in another UHV setup following removal of the selenium capping by gentle thermal annealing of the samples (between 250 and 300 °C) for 1 to 2 h. This confirms the stability of our lateral heterostructures up to these temperatures. All the STM images and spectra were acquired at ∼4.2 K using a Createc LT-STM (CreaTec GmbH), or Unisoku USM-1300 (Unisoku Co., Ltd.) at 2 K (Figure 1d). For STM topography images, feedback set-point bias voltage (V_s) and tunneling current (I_t) are given in the figure captions. Topography images are rendered with Gwyddion.[60] Scanning tunneling spectra (STS) or differential conductance (dI/dV) spectroscopy are measured with the lock-in technique at the frequency of 746 Hz, and the peak-to-peak modulation voltage (V_{mod}) is specified in the figure caption.

Density Functional Theory Calculations. DFT calculations were performed with the *QUANTUM ESPRESSO* distribution.[61] Interaction between electrons and ions were described with the PAW pseudopotentials,[62,63] while the electronic wave functions were expanded considering a plane-wave basis set with kinetic energy cutoffs of 90 Ry. For the lateral heterostructures, the integration over

https://doi.org/10.1021/acsnano.4c10302
ACS Nano 2024, 18, 31300−31308

the Brillouin zone (BZ) was performed using a uniform grid of 1 × 8 × 1 k-point. For the results shown in the main paper, we have adopted the standard Perdew−Burke−Ernzerhof (PBE) functional augmented with + U correction of 2 eV on V-3d orbitals.[64,65] Results with other values of + U are present in the SI. STM simulations, and LDOS maps were obtained with the *critic2* code.[66,67]

ASSOCIATED CONTENT

Supporting Information

The Supporting Information is available free of charge at https://pubs.acs.org/doi/10.1021/acsnano.4c10302.

Additional STM data on growth of heterostructures, CDW orientations and Kondo resonances, additional RHEED data including lattice constant determination, and detailed DFT calculations (PDF)

AUTHOR INFORMATION

Corresponding Author

Jani Sainio − *Department of Applied Physics, Aalto University, FI-00076 Aalto, Finland;* orcid.org/0000-0002-4435-0016; Email: jani.sainio@aalto.fi

Authors

Xin Huang − *Department of Applied Physics, Aalto University, FI-00076 Aalto, Finland;* orcid.org/0009-0003-9409-3921

Héctor González-Herrero − *Department of Applied Physics, Aalto University, FI-00076 Aalto, Finland; Departamento Física de la Materia Condensada, Universidad Autónoma de Madrid, Madrid E-28049, Spain;* orcid.org/0000-0002-3028-9875

Orlando J. Silveira − *Department of Applied Physics, Aalto University, FI-00076 Aalto, Finland;* orcid.org/0000-0002-0403-9485

Shawulienu Kezilebieke − *Department of Physics, Department of Chemistry and Nanoscience Center, University of Jyväskylä, FI-40014 Jyväskylä, Finland;* orcid.org/0000-0003-4166-5079

Peter Liljeroth − *Department of Applied Physics, Aalto University, FI-00076 Aalto, Finland;* orcid.org/0000-0003-1253-8097

Complete contact information is available at: https://pubs.acs.org/10.1021/acsnano.4c10302

Author Contributions

X.H. and H.G.H. contributed equally to this work. X.H., S.K., and P.L. conceived the idea and designed the experiment. X.H. and H.G.-H. assembled the MBE and synthesized materials and performed STM measurements. O.J.S. and X.H. performed DFT calculations. X.H. analyzed STM data. X.H., H.G.-H., J.S., and P.L. composed the manuscript, and all authors discussed the results and commented on the manuscript.

Notes

The authors declare no competing financial interest.

ACKNOWLEDGMENTS

This research made use of the Aalto Nanomicroscopy Center (Aalto NMC) facilities and was supported by the European Research Council (ERC-2017-AdG no. 788185 "Artificial Designer Materials") and Academy of Finland (Academy professor funding nos. 318995 and 320555, Academy research fellow nos. 338478 and 346654). Computing resources from the Aalto Science-IT project and CSC, Helsinki, are gratefully acknowledged. X.H. thanks Mr. HUANG Ruojun and Mrs. XIONG Dongyan. H.G-H. acknowledges financial support from the Spanish State Research Agency under grant Ramón y Cajal fellowship RYC2021-031050-I.

REFERENCES

(1) Geim, A. K.; Grigorieva, I. V. van der Waals Heterostructures. *Nature* **2013**, *499*, 519−525.

(2) Novoselov, K. S.; Mishchenko, A.; Carvalho, A.; Castro Neto, A. H. 2D Materials and van der Waals Heterostructures. *Science* **2016**, *353*, No. aac9439.

(3) Castellanos-Gomez, A.; Duan, X.; Fei, Z.; Gutierrez, H. R.; Huang, Y.; Huang, X.; Quereda, J.; Qian, Q.; Sutter, E.; Sutter, P. van der Waals Heterostructures. *Nat. Rev. Methods Primers* **2022**, *2*, 57.

(4) Barja, S.; Wickenburg, S.; Liu, Z.-F.; Zhang, Y.; Ryu, H.; Ugeda, M. M.; Hussain, Z.; Shen, Z.-X.; Mo, S.-K.; Wong, E.; Salmeron, M. B.; Wang, F.; Crommie, M. F.; Ogletree, D. F.; Neaton, J. B.; Weber-Bargioni, A. Charge Density Wave Order in 1D Mirror Twin Boundaries of Single-Layer $MoSe_2$. *Nat. Phys.* **2016**, *12*, 751−756.

(5) Yin, L. J.; Jiang, H.; Qiao, J. B.; He, L. Direct Imaging of Topological Edge States at a Bilayer Graphene Domain Wall. *Nat. Commun.* **2016**, *7*, No. 11760.

(6) Cho, D.; Gye, G.; Lee, J.; Lee, S. H.; Wang, L.; Cheong, S. W.; Yeom, H. W. Correlated Electronic States at Domain Walls of a Mott-Charge-Density-Wave Insulator 1T-TaS_2. *Nat. Commun.* **2017**, *8*, No. 392.

(7) Yuan, Y.; Li, W.; Liu, B.; Deng, P.; Xu, Z.; Chen, X.; Song, C.; Wang, L.; He, K.; Xu, G.; Ma, X.; Xue, Q. K. Edge States at Nematic Domain Walls in FeSe Films. *Nano Lett.* **2018**, *18*, 7176−7180.

(8) Duan, X.; Wang, C.; Shaw, J. C.; Cheng, R.; Chen, Y.; Li, H.; Wu, X.; Tang, Y.; Zhang, Q.; Pan, A.; Jiang, J.; Yu, R.; Huang, Y.; Duan, X. Lateral Epitaxial Growth of Two-Dimensional Layered Semiconductor Heterojunctions. *Nat. Nanotechnol.* **2014**, *9*, 1024−1030.

(9) Huang, C.; Wu, S.; Sanchez, A. M.; Peters, J. J.; Beanland, R.; Ross, J. S.; Rivera, P.; Yao, W.; Cobden, D. H.; Xu, X. Lateral Heterojunctions Within Monolayer $MoSe_2$-WSe_2 Semiconductors. *Nat. Mater.* **2014**, *13*, 1096−1101.

(10) Gong, Y.; Lin, J.; Wang, X.; Shi, G.; Lei, S.; Lin, Z.; Zou, X.; Ye, G.; Vajtai, R.; Yakobson, B. I.; Terrones, H.; Terrones, M.; Tay, B. K.; Lou, J.; Pantelides, S. T.; Liu, Z.; Zhou, W.; Ajayan, P. M. Vertical and In-Plane Heterostructures from WS_2/MoS_2 Monolayers. *Nat. Mater.* **2014**, *13*, 1135−1142.

(11) Lin, Y. C.; Dumcenco, D. O.; Huang, Y. S.; Suenaga, K. Atomic Mechanism of the Semiconducting-to-Metallic Phase Transition in Single-Layered MoS_2. *Nat. Nanotechnol.* **2014**, *9*, 391−396.

(12) Li, M. Y.; Shi, Y.; Cheng, C. C.; Lu, L. S.; Lin, Y. C.; Tang, H. L.; Tsai, M. L.; Chu, C. W.; Wei, K. H.; He, J. H.; Chang, W. H.; Suenaga, K.; Li, L. J. Epitaxial Growth of a Monolayer WSe_2-MoS_2 Lateral p-n Junction with an Atomically Sharp Interface. *Science* **2015**, *349*, 524−528.

(13) Zhang, Z.; Chen, P.; Duan, X.; Zang, K.; Luo, J.; Duan, X. Robust Epitaxial Growth of Two-Dimensional Heterostructures, Multiheterostructures, and Superlattices. *Science* **2017**, *357*, 788−792.

(14) Sahoo, P. K.; Memaran, S.; Xin, Y.; Balicas, L.; Gutierrez, H. R. One-Pot Growth of Two-Dimensional Lateral Heterostructures via Sequential Edge-Epitaxy. *Nature* **2018**, *553*, 63−67.

(15) Zhang, C.; Li, M. Y.; Tersoff, J.; Han, Y.; Su, Y.; Li, L. J.; Muller, D. A.; Shih, C. K. Strain Distributions and Their Influence on Electronic Structures of WSe_2-MoS_2 Laterally Strained Heterojunctions. *Nat. Nanotechnol.* **2018**, *13*, 152−158.

(16) Lin, Y. C.; Yeh, C. H.; Lin, H. C.; Siao, M. D.; Liu, Z.; Nakajima, H.; Okazaki, T.; Chou, M. Y.; Suenaga, K.; Chiu, P. W. Stable 1T Tungsten Disulfide Monolayer and Its Junctions: Growth and Atomic Structures. *ACS Nano* **2018**, *12*, 12080−12088.

(17) Wang, J.; Li, Z.; Chen, H.; Deng, G.; Niu, X. Recent Advances in 2D Lateral Heterostructures. *Nano-Micro Lett.* **2019**, *11*, 48.

(18) Zhang, R.; Li, M.; Li, L.; Wei, Z.; Jiao, F.; Geng, D.; Hu, W. The More, the Better—Recent Advances in Construction of 2D Multi-Heterostructures. *Adv. Funct. Mater.* **2021**, *31*, No. 2102049.
(19) Avalos-Ovando, O.; Mastrogiuseppe, D.; Ulloa, S. E. Lateral Heterostructures and One-Dimensional Interfaces in 2D Transition Metal Dichalcogenides. *J. Phys.: Condens. Matter* **2019**, *31*, 213001.
(20) Chen, K.; Wan, X.; Xie, W.; Wen, J.; Kang, Z.; Zeng, X.; Chen, H.; Xu, J. Lateral Built-In Potential of Monolayer MoS_2-WS_2 In-Plane Heterostructures by a Shortcut Growth Strategy. *Adv. Mater.* **2015**, *27*, 6431−6437.
(21) Liu, M.; Gou, J.; Liu, Z.; Chen, Z.; Ye, Y.; Xu, J.; Xu, X.; Zhong, D.; Eda, G.; Wee, A. T. S. Phase-Selective In-Plane Heteroepitaxial Growth of H-phase $CrSe_2$. *Nat. Commun.* **2024**, *15*, No. 1765.
(22) Feng, J.; Biswas, D.; Rajan, A.; Watson, M. D.; Mazzola, F.; Clark, O. J.; Underwood, K.; Marković, I.; McLaren, M.; Hunter, A.; Burn, D. M.; Duffy, L. B.; Barua, S.; Balakrishnan, G.; Bertran, F.; Fèvre, P. L.; Kim, T. K.; van der Laan, G.; Hesjedal, T.; Wahl, P.; et al. Electronic Structure and Enhanced Charge-Density Wave Order of Monolayer VSe_2. *Nano Lett.* **2018**, *18*, 4493−4499.
(23) Coelho, P. M.; Nguyen Cong, K.; Bonilla, M.; Kolekar, S.; Phan, M.-H.; Avila, J.; Asensio, M. C.; Oleynik, I. I.; Batzill, M. Charge Density Wave State Suppresses Ferromagnetic Ordering in VSe_2 Monolayers. *J. Phys. Chem. C* **2019**, *123*, 14089−14096.
(24) Wong, P. K. J.; Zhang, W.; Bussolotti, F.; Yin, X.; Herng, T. S.; Zhang, L.; Huang, Y. L.; Vinai, G.; Krishnamurthi, S.; Bukhvalov, D. W.; Zheng, Y. J.; Chua, R.; N'Diaye, A. T.; Morton, S. A.; Yang, C.-Y.; Yang, K.-H. O.; Torelli, P.; Chen, W.; Goh, K. E. J.; Ding, J.; et al. Evidence of Spin Frustration in a Vanadium Diselenide Monolayer Magnet. *Adv. Mater.* **2019**, *31*, No. 1901185.
(25) Fumega, A. O.; Gobbi, M.; Dreher, P.; Wan, W.; González-Orellana, C.; Peña-Díaz, M.; Rogero, C.; Herrero-Martín, J.; Gargiani, P.; Ilyn, M.; Ugeda, M. M.; Pardo, V.; Blanco-Canosa, S. Absence of Ferromagnetism in VSe_2 Caused by Its Charge Density Wave Phase. *J. Phys. Chem. C* **2019**, *123*, 27802−27810.
(26) Fumega, A. O.; Diego, J.; Pardo, V.; Blanco-Canosa, S.; Errea, I. Anharmonicity Reveals the Tunability of the Charge Density Wave Orders in Monolayer VSe_2. *Nano Lett.* **2023**, *23*, 1794−1800.
(27) Ma, Y.; Dai, Y.; Guo, M.; Niu, C.; Zhu, Y.; Huang, B. Evidence of the Existence of Magnetism in Pristine VX_2 Monolayers (X = S, Se) and Their Strain-Induced Tunable Magnetic Properties. *ACS Nano* **2012**, *6*, 1695−1701.
(28) Kezilebieke, S.; Huda, M. N.; Dreher, P.; Manninen, I.; Zhou, Y.; Sainio, J.; Mansell, R.; Ugeda, M. M.; van Dijken, S.; Komsa, H.-P.; Liljeroth, P. Electronic and Magnetic Characterization of Epitaxial VSe_2 Monolayers on Superconducting $NbSe_2$. *Commun. Phys.* **2020**, *3*, No. 116.
(29) Chua, R.; Yang, J.; He, X.; Yu, X.; Yu, W.; Bussolotti, F.; Wong, P. K. J.; Loh, K. P.; Breese, M. B. H.; Goh, K. E. J.; Huang, Y. L.; Wee, A. T. S. Can Reconstructed Se-Deficient Line Defects in Monolayer VSe_2 Induce Magnetism? *Adv. Mater.* **2020**, *32*, No. 2000693.
(30) Memarzadeh, S.; Roknabadi, M. R.; Modarresi, M.; Mogulkoc, A.; Rudenko, A. N. Role of Charge Doping and Strain in the Stabilization of In-Plane Ferromagnetism in monolayer VSe_2 at room temperature. *2D Mater.* **2021**, *8*, No. 035022.
(31) Ugeda, M. M.; Bradley, A. J.; Zhang, Y.; Onishi, S.; Chen, Y.; Ruan, W.; Ojeda-Aristizabal, C.; Ryu, H.; Edmonds, M. T.; Tsai, H.-Z.; Riss, A.; Mo, S.-K.; Lee, D.; Zettl, A.; Hussain, Z.; Shen, Z.-X.; Crommie, M. F. Characterization of Collective Ground States in Single-Layer $NbSe_2$. *Nat. Phys.* **2016**, *12*, 92−97.
(32) Xi, X.; Zhao, L.; Wang, Z.; Berger, H.; Forro, L.; Shan, J.; Mak, K. F. Strongly Enhanced Charge-Density-Wave Order in Monolayer $NbSe_2$. *Nat. Nanotechnol.* **2015**, *10*, 765−769.
(33) Zhao, K.; Lin, H.; Xiao, X.; Huang, W.; Yao, W.; Yan, M.; Xing, Y.; Zhang, Q.; Li, Z.-X.; Hoshino, S.; Wang, J.; Zhou, S.; Gu, L.; Bahramy, M. S.; Yao, H.; Nagaosa, N.; Xue, Q.-K.; Law, K. T.; Chen, X.; Ji, S.-H. Disorder-Induced Multifractal Superconductivity in Monolayer Niobium Dichalcogenides. *Nat. Phys.* **2019**, *15*, 904−910.
(34) Divilov, S.; Wan, W.; Dreher, P.; Bölen, E.; Sánchez-Portal, D.; Ugeda, M. M.; Ynduráin, F. Magnetic Correlations in Single-Layer $NbSe_2$. *J. Phys.: Condens. Matter* **2021**, *33*, 295804.
(35) Ganguli, S. C.; Vaňo, V.; Kezilebieke, S.; Lado, J. L.; Liljeroth, P. Confinement-Engineered Superconductor to Correlated-Insulator Transition in a van der Waals Monolayer. *Nano Lett.* **2022**, *22*, 1845−1850.
(36) Wan, W.; Dreher, P.; Muñoz-Segovia, D.; Harsh, R.; Guo, H.; Martínez-Galera, A. J.; Guinea, F.; de Juan, F.; Ugeda, M. M. Observation of Superconducting Collective Modes from Competing Pairing Instabilities in Single-Layer $NbSe_2$. *Adv. Mater.* **2022**, *34*, No. 2206078.
(37) Akber, H.; Shan, H.; Mao, Y.; Yao, J.; Zhai, X.; Zhao, A. Nonreciprocal Charge-Density-Wave Proximity Effect in a Lateral Heterojunction of $NbSe_2$/$TiSe_2$. *Appl. Phys. Lett.* **2024**, *124*, No. 071602.
(38) Liu, L.; Park, J.; Siegel, D. A.; McCarty, K. F.; Clark, K. W.; Deng, W.; Basile, L.; Idrobo, J. C.; Li, A.-P.; Gu, G. Heteroepitaxial Growth of Two-Dimensional Hexagonal Boron Nitride Templated by Graphene Edges. *Science* **2014**, *343*, 163−167.
(39) Sutter, P.; Huang, Y.; Sutter, E. Nanoscale Integration of Two-Dimensional Materials by Lateral Heteroepitaxy. *Nano Lett.* **2014**, *14*, 4846−4851.
(40) Zhou, Z.; Hou, F.; Huang, X.; Wang, G.; Fu, Z.; Liu, W.; Yuan, G.; Xi, X.; Xu, J.; Lin, J.; Gao, L. Stack Growth of Wafer-Scale van der Waals Superconductor Heterostructures. *Nature* **2023**, *621*, 499−505.
(41) Chen, P.; Pai, W. W.; Chan, Y.-H.; Madhavan, V.; Chou, M. Y.; Mo, S.-K.; Fedorov, A.-V.; Chiang, T.-C. Unique Gap Structure and Symmetry of the Charge Density Wave in Single-Layer VSe_2. *Phys. Rev. Lett.* **2018**, *121*, No. 196402.
(42) Lu, J.; Bao, D. L.; Qian, K.; Zhang, S.; Chen, H.; Lin, X.; Du, S. X.; Gao, H. J. Identifying and Visualizing the Edge Terminations of Single-Layer $MoSe_2$ Island Epitaxially Grown on Au(111). *ACS Nano* **2017**, *11*, 1689−1695.
(43) Zhang, Q.; Fan, J.; Zhang, T.; Wang, J.; Hao, X.; Xie, Y.-M.; Huang, Z.; Chen, Y.; Liu, M.; Jia, L.; Yang, H.; Liu, L.; Huang, H.; Zhang, Y.; Duan, W.; Wang, Y. Visualization of Edge-Modulated Charge-Density-Wave Orders in Monolayer Transition-Metal-Dichalcogenide Metal. *Commun. Phys.* **2022**, *5*, No. 117.
(44) Silva-Guillén, J. Á.; Ordejón, P.; Guinea, F.; Canadell, E. Electronic Structure of 2H-$NbSe_2$ Single-Layers in the CDW State. *2D Mater.* **2016**, *3*, No. 035028.
(45) Pásztor, A.; Scarfato, A.; Barreteau, C.; Giannini, E.; Renner, C. Dimensional Crossover of the Charge Density Wave Transition in Thin Exfoliated VSe_2. *2D Mater.* **2017**, *4*, No. 041005.
(46) Jolie, W.; Knispel, T.; Ehlen, N.; Nikonov, K.; Busse, C.; Grüneis, A.; Michely, T. Charge Density Wave Phase of VSe_2 Revisited. *Phys. Rev. B* **2019**, *99*, No. 115417.
(47) Chen, Y.; Zhang, Y.; Wang, W.; Song, X.; Jia, L. G.; Zhang, C.; Zhou, L.; Han, X.; Yang, H. X.; Liu, L. W.; Si, C.; Gao, H. J.; Wang, Y. L. Visualization of Confined Electrons at Grain Boundaries in a Monolayer Charge-Density-Wave Metal. *Adv. Sci.* **2023**, *11*, No. e2306171.
(48) Crommie, M.; Lutz, C.; Eigler, D. Imaging Standing Waves in a Two-Dimensional Electron Gas. *Nature* **1993**, *363*, 524−527.
(49) Ternes, M. Spin Excitations and Correlations in Scanning Tunneling Spectroscopy. *New J. Phys.* **2015**, *17*, No. 063016.
(50) Choi, D.-J.; Lorente, N.; Wiebe, J.; von Bergmann, K.; Otte, A. F.; Heinrich, A. J. Colloquium: Atomic Spin Chains on Surfaces. *Rev. Mod. Phys.* **2019**, *91*, No. 041001.
(51) Ganguli, S. C.; Aapro, M.; Kezilebieke, S.; Amini, M.; Lado, J. L.; Liljeroth, P. Visualization of Moiré Magnons in Monolayer Ferromagnet. *Nano Lett.* **2023**, *23*, 3412−3417.
(52) Liu, Z.-L.; Wu, X.; Shao, Y.; Qi, J.; Cao, Y.; Huang, L.; Liu, C.; Wang, J.-O.; Zheng, Q.; Zhu, Z.-L.; Ibrahim, K.; Wang, Y.-L.; Gao, H.-J. Epitaxially Grown Monolayer VSe_2: An Air-Stable Magnetic Two-Dimensional Material with Low Work Function at Edges. *Science Bulletin* **2018**, *63*, 419−425.

https://doi.org/10.1021/acsnano.4c10302
ACS Nano 2024, 18, 31300−31308

(53) Esters, M.; Hennig, R. G.; Johnson, D. C. Dynamic Instabilities in Strongly Correlated VSe_2 Monolayers and Bilayers. *Phys. Rev. B* **2017**, *96*, No. 235147.
(54) Yin, L.; Berlijn, T.; Juneja, R.; Lindsay, L.; Parker, D. S. Competing Magnetic and Nonmagnetic States in Monolayer VSe_2 with Charge Density Wave. *Phys. Rev. B* **2022**, *106*, No. 085117.
(55) Grobis, M.; Rau, I. G.; Potok, R. M.; Goldhaber-Gordon, D. *Handbook of Magnetism and Advanced Magnetic Materials*; John Wiley & Sons, Ltd., 2007.
(56) Sasaki, S.; Tamura, H.; Akazaki, T.; Fujisawa, T. Fano-Kondo Interplay in a Side-Coupled Double Quantum Dot. *Phys. Rev. Lett.* **2009**, *103*, No. 266806.
(57) Hur, K. L. Quantum Dots and the Kondo Effect. *Nature* **2015**, *526*, 203−204.
(58) Spera, M.; Scarfato, A.; Pasztor, A.; Giannini, E.; Bowler, D. R.; Renner, C. Insight into the Charge Density Wave Gap from Contrast Inversion in Topographic STM Images. *Phys. Rev. Lett.* **2020**, *125*, No. 267603.
(59) Pasztor, A.; Scarfato, A.; Spera, M.; Flicker, F.; Barreteau, C.; Giannini, E.; Wezel, J. V.; Renner, C. Multiband Charge Density Wave Exposed in a Transition Metal Dichalcogenide. *Nat. Commun.* **2021**, *12*, No. 6037.
(60) Nečas, D.; Klapetek, P. Gwyddion: An Open-Source Software for SPM Data Analysis. *Open Phys.* **2012**, *10*, 181−188.
(61) Giannozzi, P.; Baroni, S.; Bonini, N.; Calandra, M.; Car, R.; Cavazzoni, C.; Ceresoli, D.; Chiarotti, G. L.; Cococcioni, M.; Dabo, I.; Corso, A. D.; de Gironcoli, S.; Fabris, S.; Fratesi, G.; Gebauer, R.; Gerstmann, U.; Gougoussis, C.; Kokalj, A.; Lazzeri, M.; Martin-Samos, L.; et al. QUANTUM ESPRESSO: A Modular and Open-Source Software Project for Quantum Simulations of Materials. *J. Phys.: Condens. Matter* **2009**, *21*, No. 395502.
(62) Klimeš, J. c. v.; Bowler, D. R.; Michaelides, A. van der Waals Density Functionals Applied to Solids. *Phys. Rev. B* **2011**, *83*, No. 195131.
(63) Dion, M.; Rydberg, H.; Schröder, E.; Langreth, D. C.; Lundqvist, B. I. van der Waals Density Functional for General Geometries. *Phys. Rev. Lett.* **2004**, *92*, No. 246401.
(64) Perdew, J. P.; Burke, K.; Ernzerhof, M. Generalized Gradient Approximation Made Simple. *Phys. Rev. Lett.* **1996**, *77*, 3865−3868.
(65) Cococcioni, M.; de Gironcoli, S. Linear Response Approach to the Calculation of the Effective Interaction Parameters in the *LDA + U* Method. *Phys. Rev. B* **2005**, *71*, No. 035105.
(66) Otero-de-la-Roza, A.; Johnson, E. R.; Luaña, V. Critic2: A Program for Real-Space Analysis of Quantum Chemical Interactions in Solids. *Comput. Phys. Commun.* **2014**, *185*, 1007−1018.
(67) Otero-de-la-Roza, A.; Blanco, M. A.; Pendás, A. M.; Luaña, V. Critic: A New Program for the Topological Analysis of Solid-State Electron Densities. *Comput. Phys. Commun.* **2009**, *180*, 157−166.

https://doi.org/10.1021/acsnano.4c10302
ACS Nano 2024, 18, 31300−31308

Supporting Information:

Atomically sharp 1D interfaces in 2D lateral heterostructures of VSe_2—$NbSe_2$ monolayers

Xin Huang,[†,§] Héctor González-Herrero,[†,‡,§] Orlando J. Silveira,[†] Shawulienu Kezilebieke,[¶] Peter Liljeroth,[†] and Jani Sainio[*,†]

†*Department of Applied Physics, Aalto University, FI-00076 Aalto, Finland*

‡*Departamento Física de la Materia Condensada, Universidad Autónoma de Madrid, Madrid E-28049, Spain*

¶*Department of Physics, Department of Chemistry and Nanoscience Center, University of Jyväskylä, FI-40014 University of Jyväskylä, Finland*

§*These two authors contributed equally*

E-mail: jani.sainio@aalto.fi

Experimental section

Figure S1 shows height data for our VSe_2–$NbSe_2$ heterostructures indicating that our lateral structures are monolayers. The obtained apparent height is 0.92 nm for the 1T-VSe_2 layer and 0.90 nm for the 1H-$NbSe_2$ layer. These values are in good agreement with other STM studies of VSe_2/HOPG: 0.85 nm;[S1] $NbSe_2$/HOPG (or graphene): about 0.7 nm[S2,S3] keeping in mind that the apparent heights depend on the bias set-point and only roughly reflect the actual height of the layers. The lateral interface between VSe_2 and $NbSe_2$ is found to be very smooth with a height difference of only 20 pm. Fig. S2 shows large area topographic data on our heterostructures as well as typical charge density waves of individual areas of the sample. From the topographic data one can observe that 1H-$NbSe_2$ islands have preferred growth directions on HOPG. Upon closer examination one finds two preferred orientations of 1H-$NbSe_2$ islands with a 30° rotation between them (also seen in main text Fig. 1).

Figures S3 and S4 (and main text Figure 1) show RHEED patterns of 1T-VSe_2, 1H-$NbSe_2$ and the 1T-VSe_2—1H-$NbSe_2$ heterostructure. The RHEED patterns do not show constant streak distances. This indicates the presence of rotational domains which occur naturally in HOPG.[S4] In addition, the previously mentioned two preferred growth directions of $NbSe_2$ will produce the same effect in the RHEED pattern. We have determined the lattice constants from these RHEED patters as indicated in Figure S4 by measuring the streak distances with respect to HOPG.

Next we focus on the interfaces of the 1T-VSe_2—1H-$NbSe_2$ lateral heterostructures. Figure S5 shows a STM image of one interface with fast Fourier transforms (FFTs) of areas near the interface on both sides. Figure S5c is the FFT of 1T-VSe_2 with exhibits typical 1×1 spots (circled in yellow) and CDW related spots (circled in blue). Figure S5e shows the FFT of 1H-$NbSe_2$ with its typical 3×3 CDW. The atomic resolution STM images and their FFT both support the observation that the two materials retain their regular structure right up to the interface.

For 1T-VSe_2, we find different CDW orientations with respect to the interfaces where

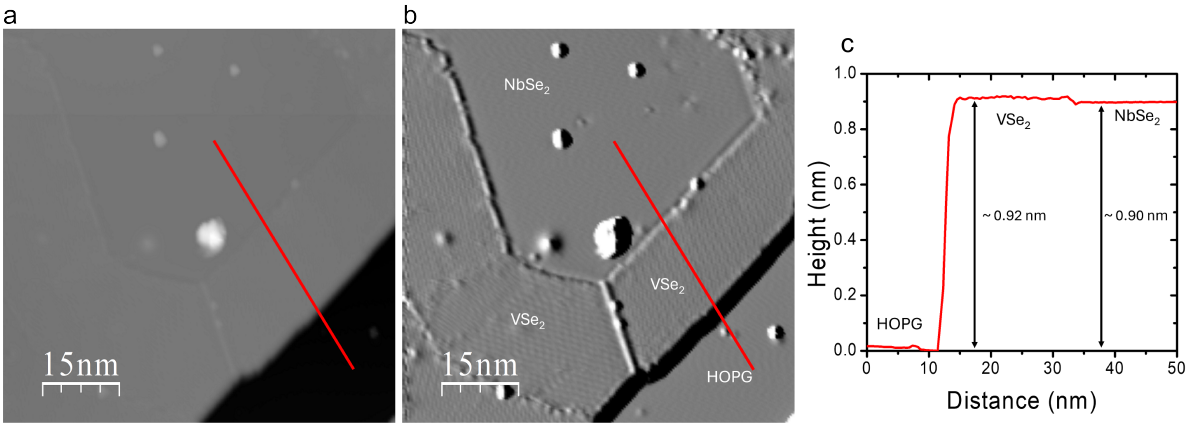

Fig. S1: Monolayer VSe_2 and $NbSe_2$ height data. **a**, STM image of a region of our VSe_2-$NbSe_2$ lateral heterostructures sample. (V_S=-1.5V; I_t=10pA). **b**, Same image as panel **a** where a derivative filter has been used to better differentiate the VSe_2 and $NbSe_2$ regions on the image. **c**, Height profile along the red line marked in panels **a** and **b** showing the height of VSe_2 and $NbSe_2$ monolayers.

the CDW "stripes" are approximately perpendicular to the interface or at an angle of 30°/150° (see Figs. S5–S10). Thus, there seems to be a preferred nucleation direction for the 1T-VSe_2 CDW and the observed angles are only a result of the spreading of the VSe_2 layer to other edges/islands. As mentioned before, there can be two growth orientations for 1H-$NbSe_2$ which will add more complexity to the possible CDW directions. In areas where rotated domains of the 1T-VSe_2 CDW meet we observe grain boundaries, as seen *e.g.* in Figs. S7 and S9. For 1H-$NbSe_2$ we occasionally observe stripe–like areas of the CDW in stead of the normal 3×3 structure (see *e.g.* Fig. S6). These have been previously shown to be caused by even small amounts of strain.[S5–S7] However, since we mostly observe areas with unperturbed 3×3 CDW contrast, the strain would not seem to be uniform throughout the $NbSe_2$ islands.

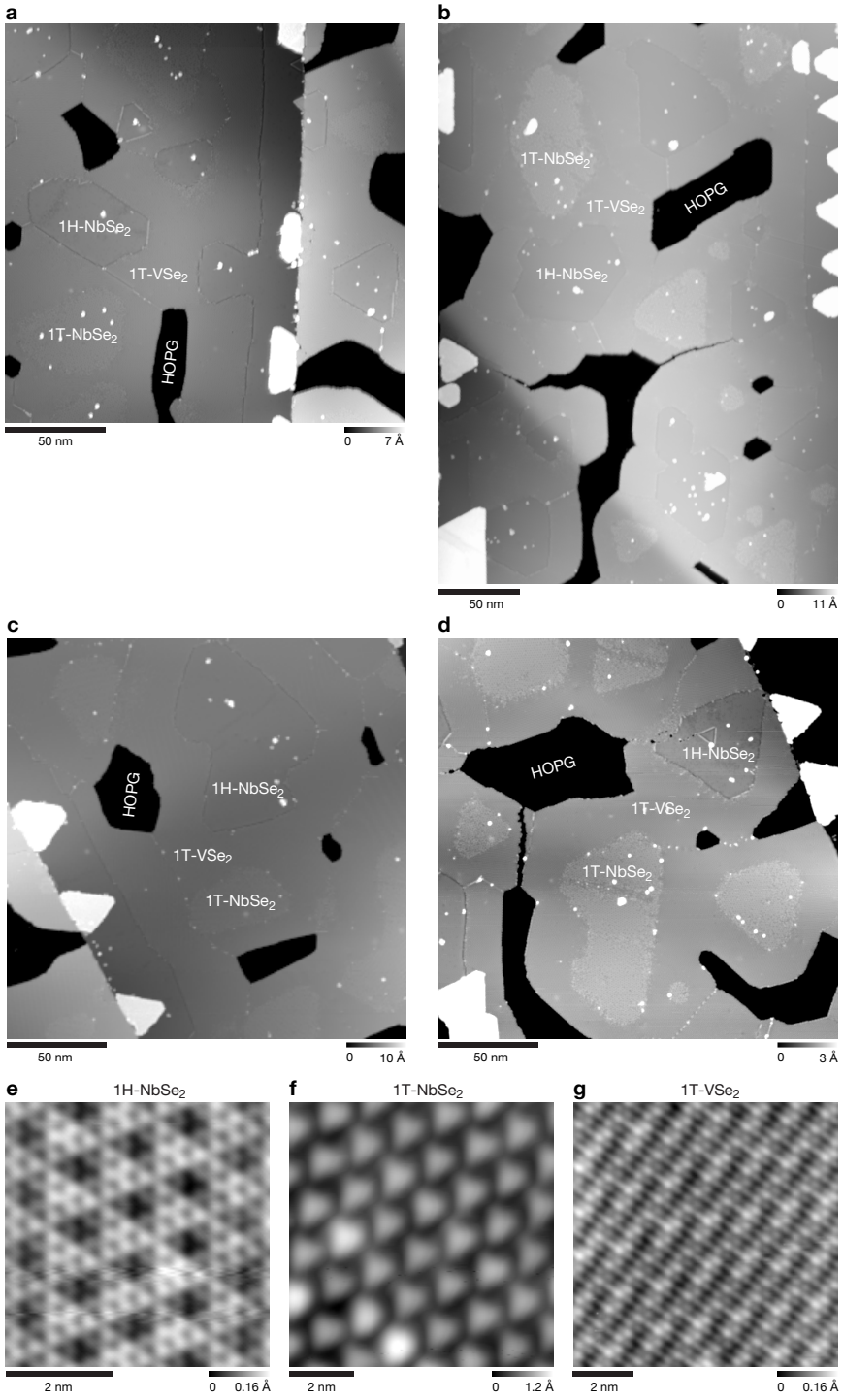

Fig. S2: Lateral heteroepitaxy protocol: VSe_2 preferentially grows laterally from the edges of $NbSe_2$ islands, rather than exhibting vertical growth. During the $NbSe_2$ growth step, both phases 1H- and 1T-$NbSe_2$ can be found and consequently, we form lateral heterostructures of the two $NbSe_2$ phases with 1T-VSe_2. **a**–**d**, Large-scale STM topography images of several different regions of the sample. Typical charge density wave of **e**, 1H-$NbSe_2$; **f**, 1T-$NbSe_2$; **g**, 1T-VSe_2, from STM topography image. Scan parameters: **a**, V_s=+1.36 V, I_t=10 pA. **b**, V_s=−1.5 V, I_t=10 pA. **c**, V_s=+1.541 V, I_t=6.5 pA. **d**, V_s=+1.5 V, I_t=4.1 pA. **e**, V_s=−0.36 V, I_t=100 pA. **f**, V_s=−0.649 V, I_t=400 pA. **g**, V_s=−1 V, I_t=100 pA.

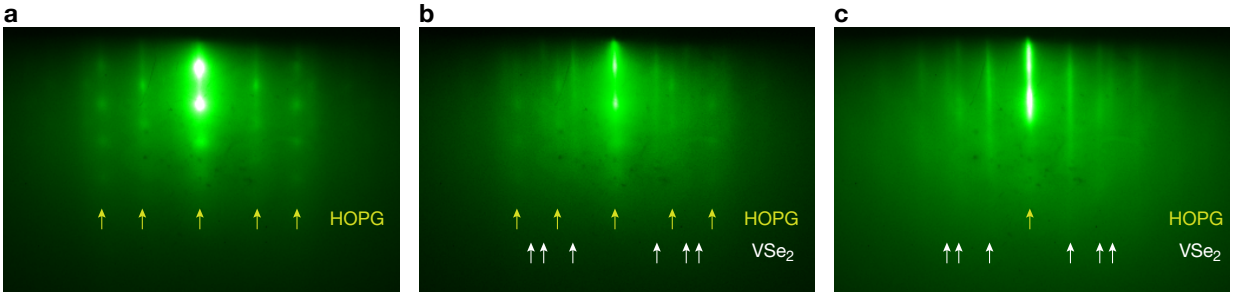

Fig. S3: Reflection high-energy electron diffraction (RHEED) pattern during the growth of monolayer VSe_2. **a**, Before the growth, RHEED pattern of the HOPG substrate. **b**, During the growth. VSe_2 stripes start appearing. **c**, End of growth. VSe_2 now has a high coverage, HOPG's pattern has diminished.

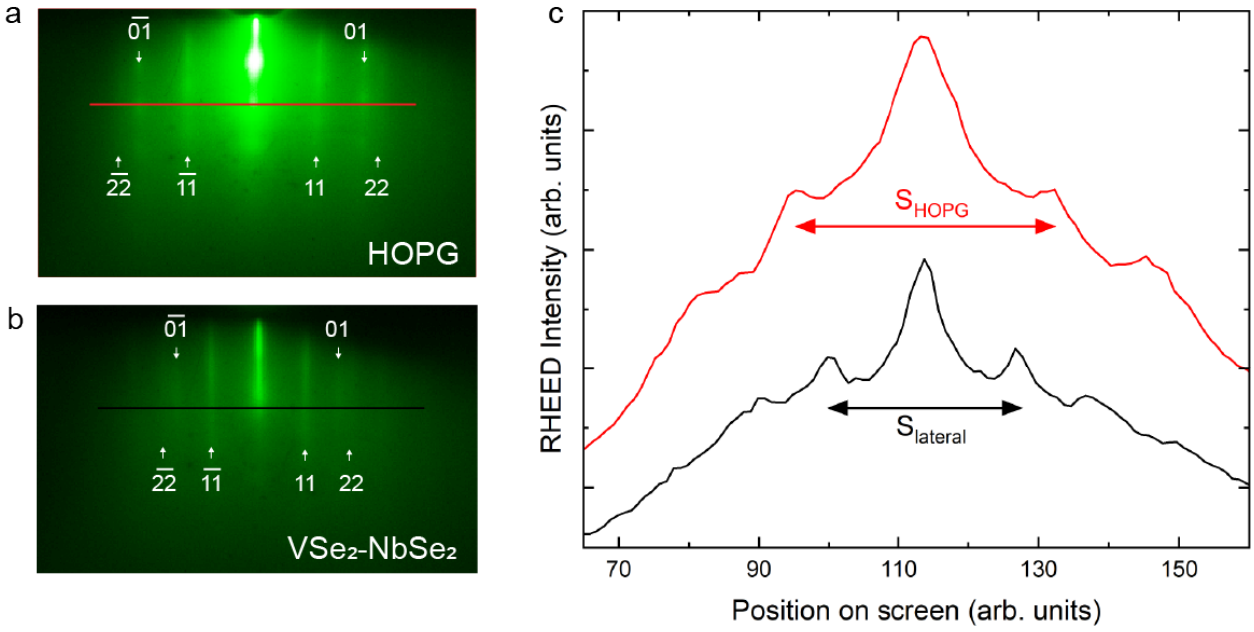

Fig. S4: An example of the determination of the lattice constant from the RHEED pattern. **a**, RHEED pattern of HOPG. **b**, RHEED pattern of the lateral VSe_2–$NbSe_2$ heterostructure. **c**, RHEED intensity line profiles for HOPG (red) and the heterostructure (black) with the streak distances S marked. The corresponding line profile positions are shown in panels **a** and **b**. From the measured streak distances the lattice constant for the heterostructure can be calculated as $(S_{HOPG}/S_{lateral}) \cdot a_{HOPG}$ where a_{HOPG} is the lattice constant of HOPG (2.46 Å).

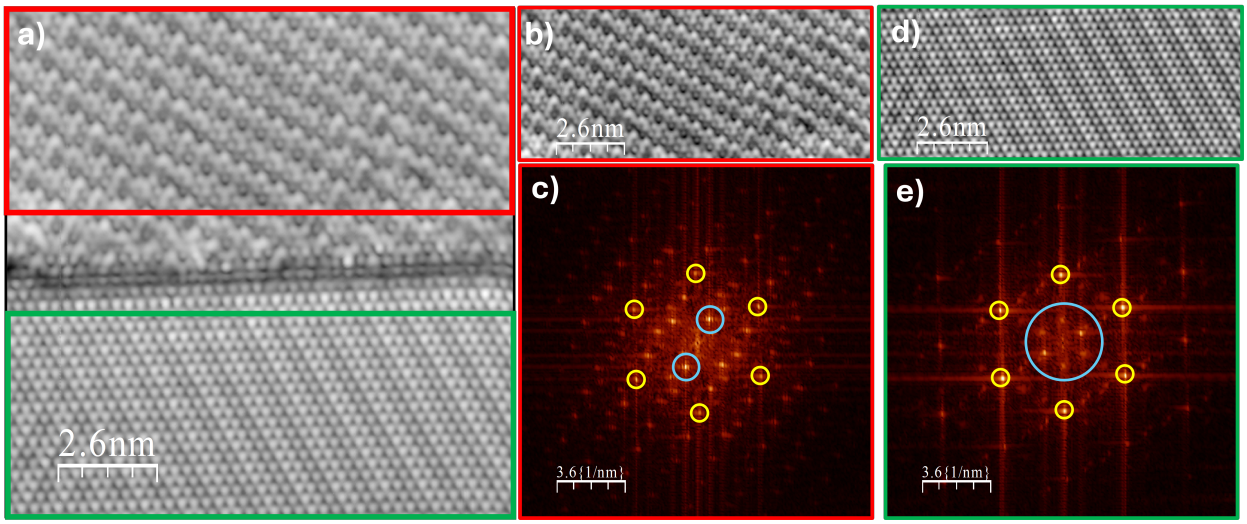

Fig. S5: FFT analysis. **a**, STM image of a 13×13 nm^2 region where an interface can be observed. **b**, Zoom in the VSe_2 part of the heterostructure. **c**, Corresponding FFT of panel b, where yellow circles mark the 1×1 lattice and the blue circles the CDW spots. **d** Zoom in the $NbSe_2$ part of the heterostructure. **e**, Corresponding FFT of panel d, where yellow circles mark the 1×1 lattice and the blue circle is around the 6 spots related with the 3×3 the CDW.

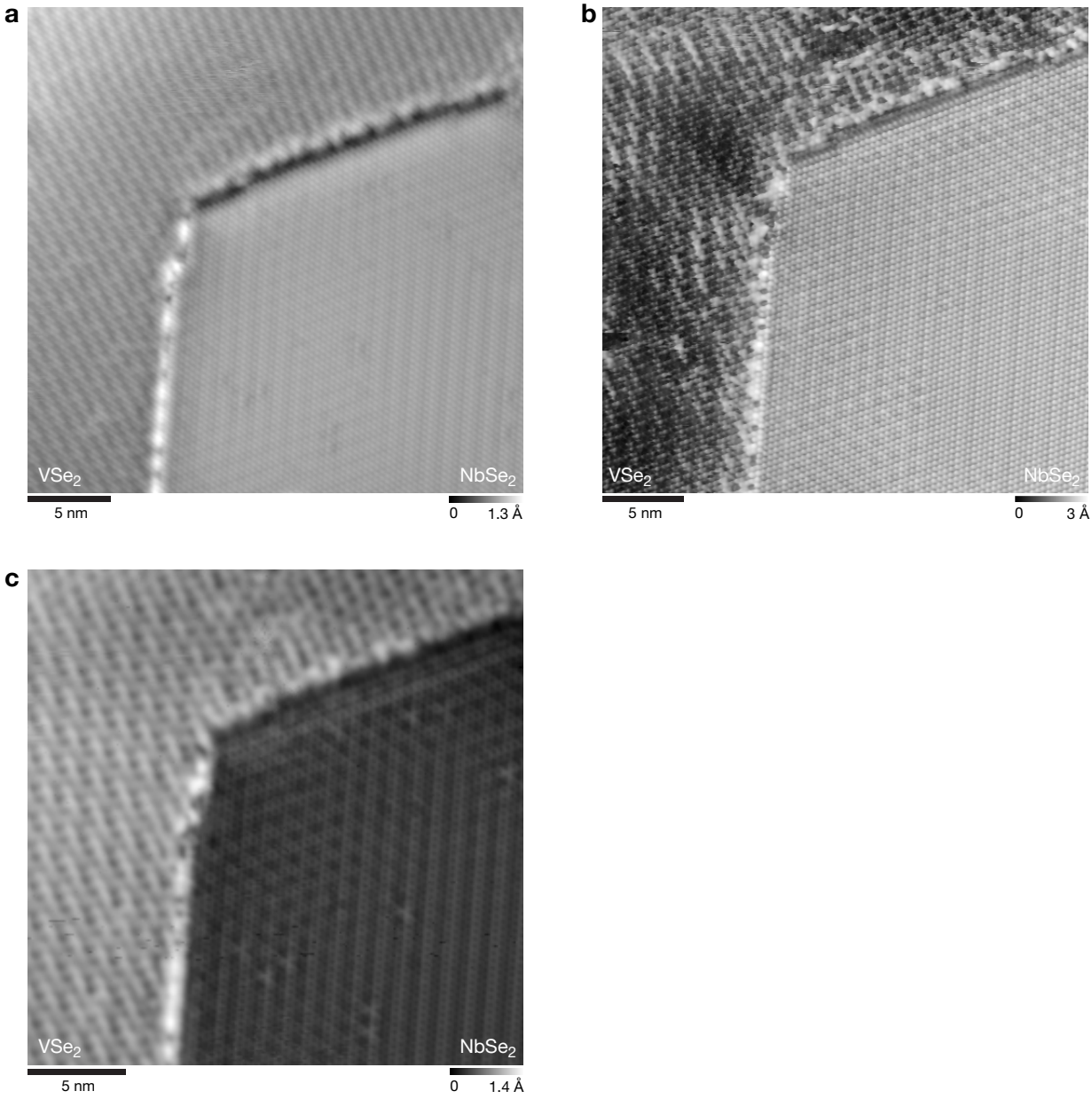

Fig. S6: Two adjacent lateral heterostructures at corner of a $NbSe_2$ island (on A-side). The interfaces shows zigzag morphology, with one of them having bright and and the other dark contrast. The intrinsic CDWs of both materials extend right up to the interface; neither the commensurate CDW of 1H-$NbSe_2$ nor the incommensurate CDW of 1T-VSe_2 extends into the other material. The length of the straight interface sections extend up to $\sim$ 20 nm. **a**, STM topography image of Fig. 2**b**, **i**, **j** and Fig. 3**h**–**j** (V_s=−1 V, I_t= 100 pA). **b**, STM image of the same area with atomic resolution (V_s=−10 mV, I_t= 790 pA). **c**, STM image of the same area showing the charge density waves (V_s=−201 mV, I_t= 50 pA).

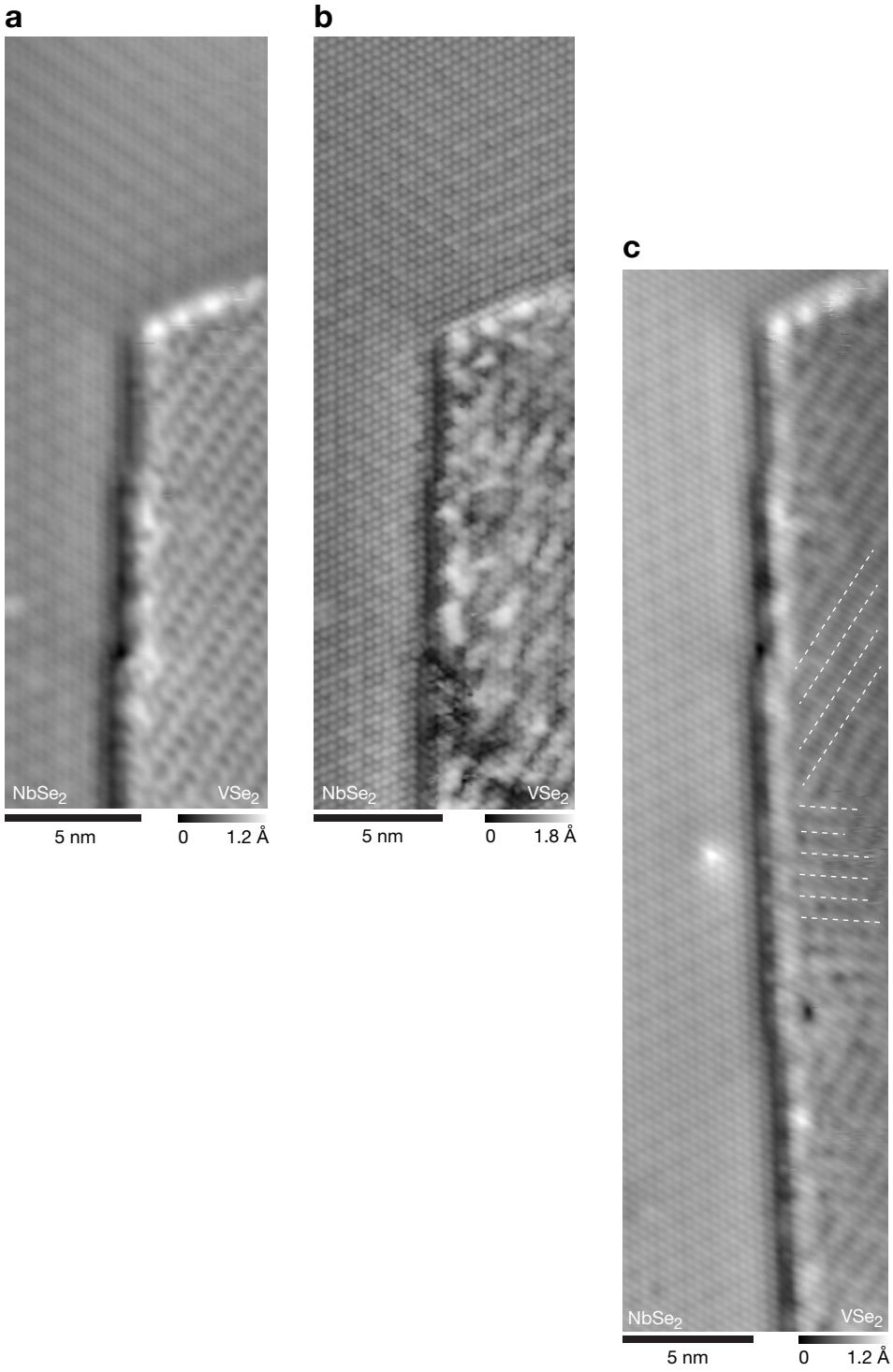

Fig. S7: Additional STM topography images of two adjacent lateral heterostructures across a corner of a $NbSe_2$ island, on A-side. Panel **a**–**c** are aligned with the same position of heterostructures. **a**, STM topography image (V_s=−1 V, I_t= 100 pA). **b**, STM topography image with atomic resolution (V_s=−10 mV, I_t= 1 nA). **c**, STM topography image. The length of the straight interface section extends up to $\sim$ 40 nm. In the middle part of the dark interface, although the CDW of 1T-VSe_2 changes its direction (indicated with dashed lines), the dark contrast of the interface does not change. (V_s=−1 V, I_t= 100 pA).

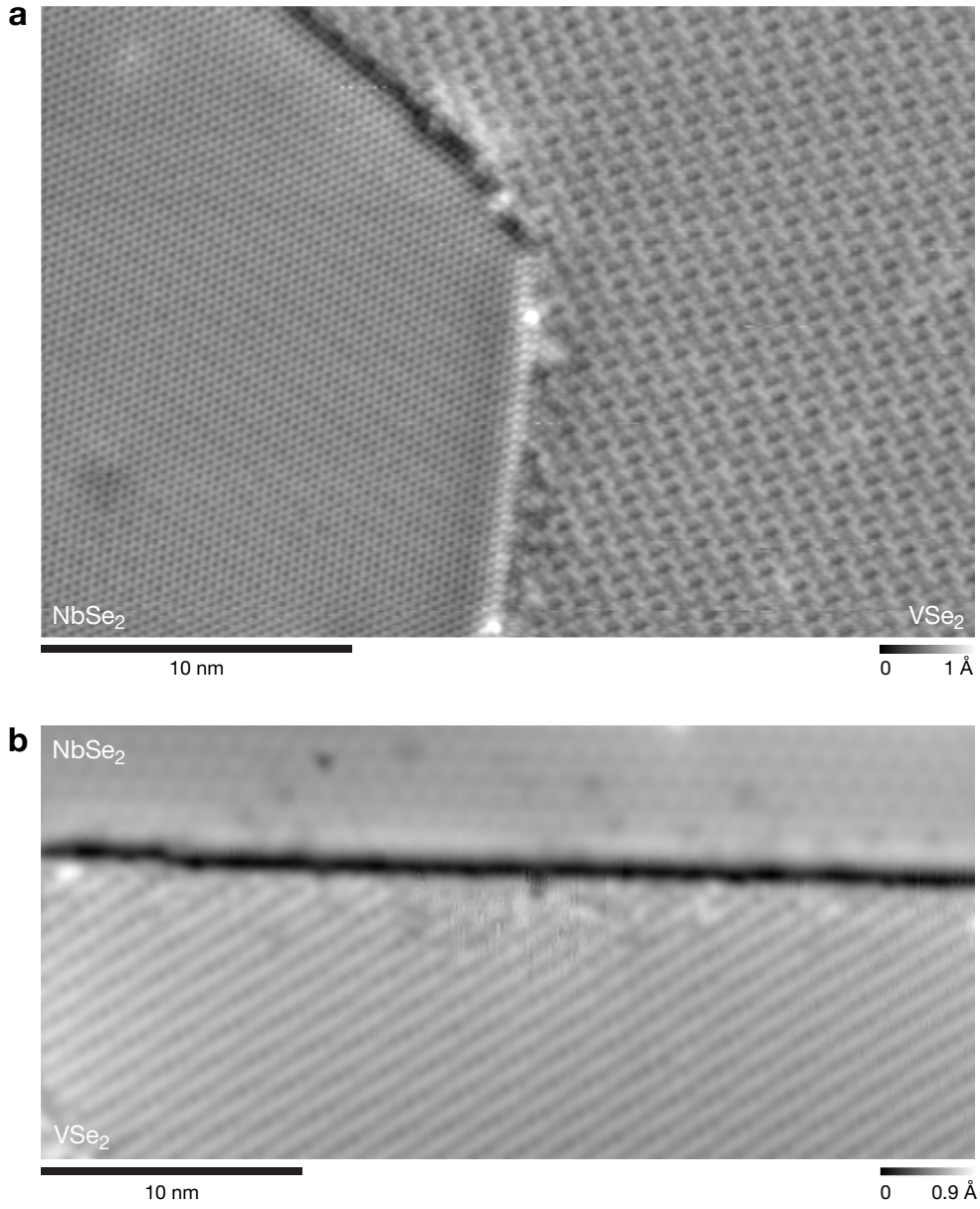

Fig. S8: **a**, Additional STM topography image of lateral heterostructures across a corner of a $NbSe_2$ island, on A-side. (V_s=−1.503 V, I_t=31 pA). **b**, Additional STM topography image of a long interface $\sim$ 36 nm (V_s=+1.36 V, I_t=90 pA).

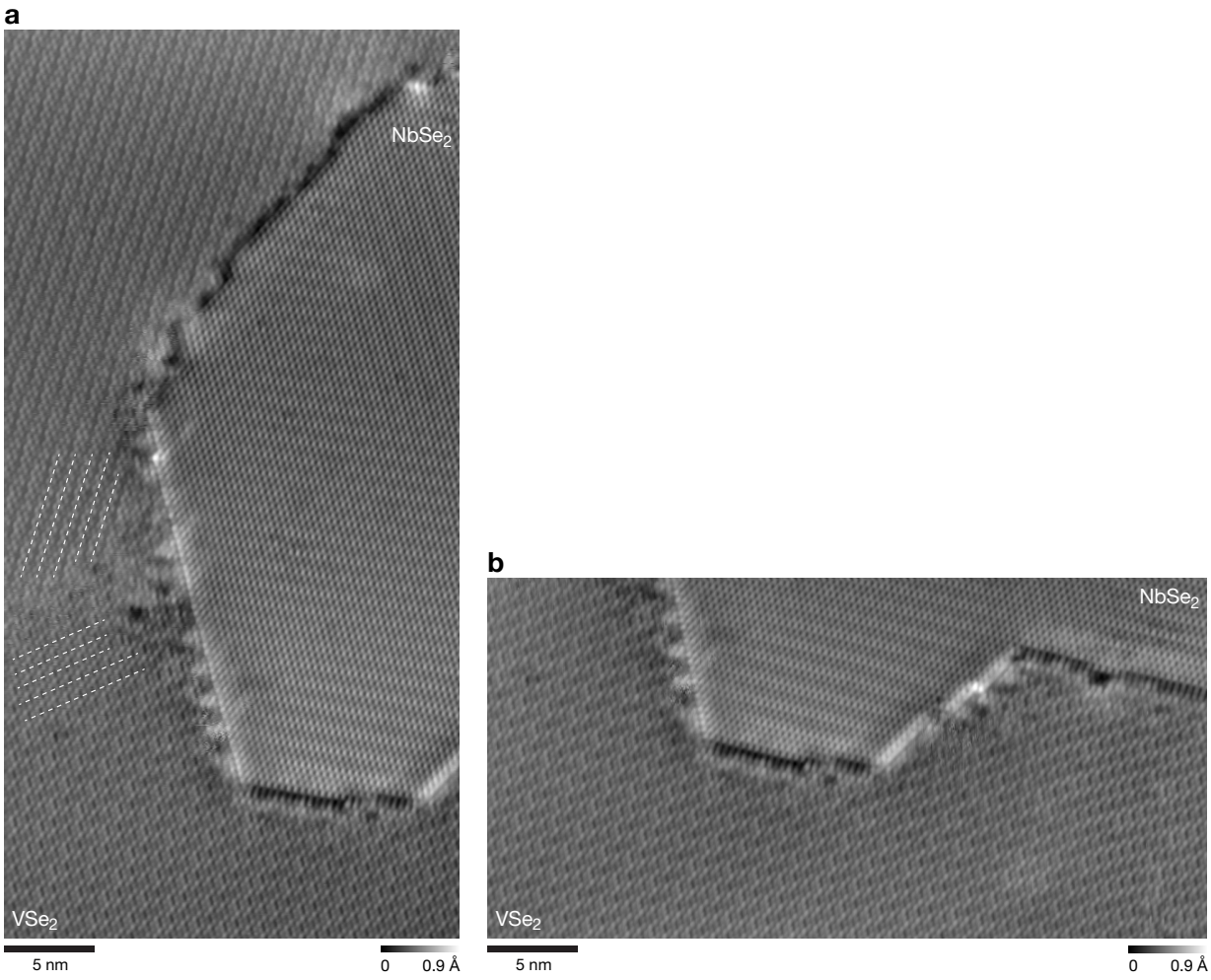

Fig. S9: Adjacent lateral heterostructures across corners of a $NbSe_2$ island, on B-side. The interfaces shows parallel morphology, and bright and dark contrast appears alternatingly at adjacent edges. **a**, STM topography image of Fig. 2**d**, **l**. Along the bright interface, in the middle, the CDW of 1T-VSe_2 changes direction (indicated with dashed lines) but the bright contrast doesn't change. (V_s=−1 V, I_t= 100 pA). **b**, Additional STM image of the same area with an extended range in the x–direction.(V_s=−1 V, I_t= 100 pA).

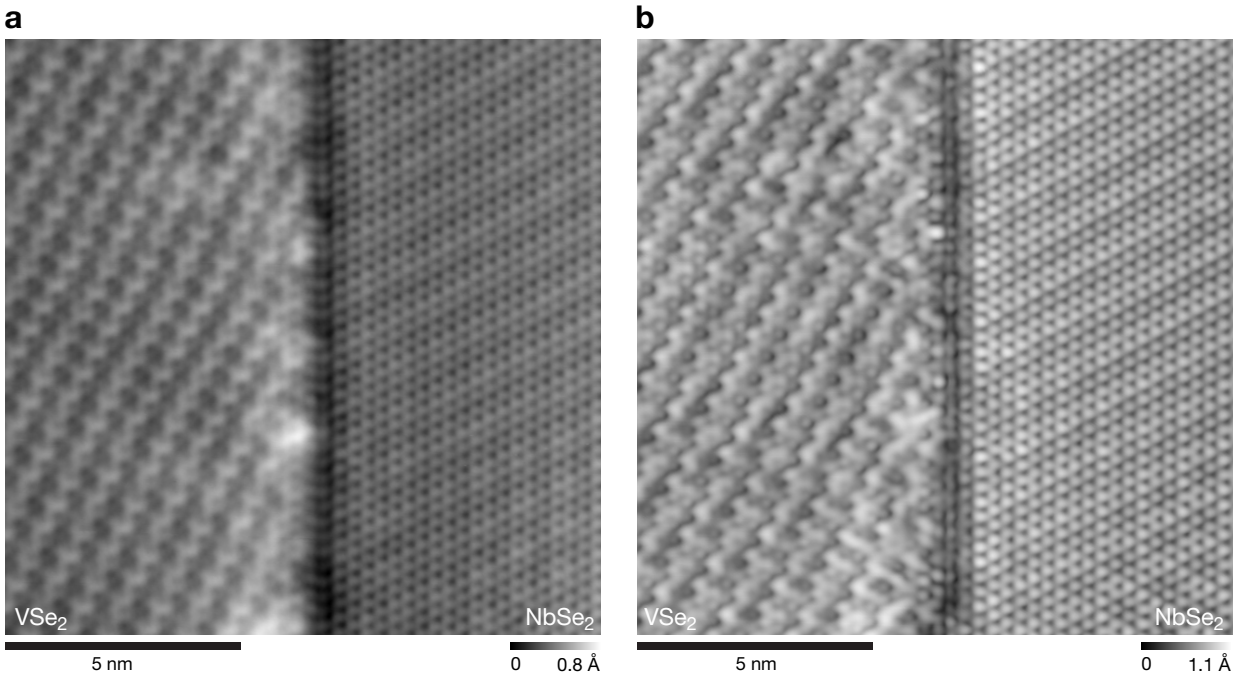

Fig. S10: VSe_5—$NbSe_6$ lateral heterostructure, on B-side. **a**, STM topography image of the interface shown in Fig. 2**k**. (V_s=−0.99 V, I_t= 50 pA). **b**, Additional STM image of the same area (V_s=−50 mV, I_t= 200 pA).

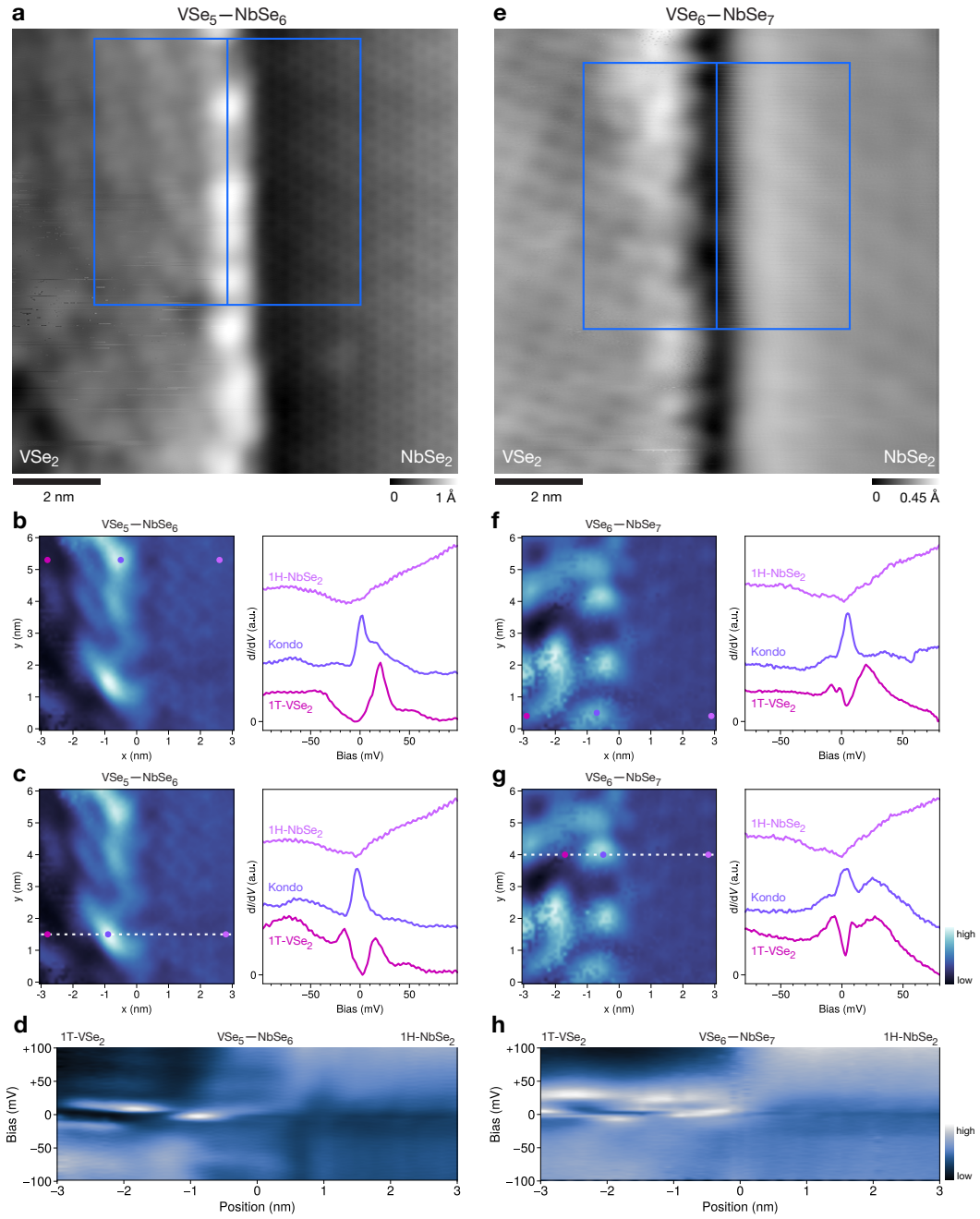

Fig. S11: Signatures of Kondo resonances in a side-coupled geometry. **a**, **e**, STM topography of VSe_5—$NbSe_6$ (Fig. 4 and Fig. 3**g**) and VSe_6—$NbSe_7$ interfaces (Fig. 4). Blue square frames indicate the dI/dV map area; the middle line indicates the 0 position of x-axis in those dI/dV maps. We do not observe defects or alloying in the mapping area. **b**, **c**, (left) dI/dV map at -0.8 mV of VSe_5—$NbSe_6$ interfaces (V_{mod}=2 mV), and (right) corresponding point dI/dV spectra (positions marked in left panel; spectra are shifted vertically for clarity; point spectra taken from the same dI/dV map). **d**, dI/dV spectra along the line indicated in **c**. **f**, **g**, (left) dI/dV map at 0 mV of VSe_6—$NbSe_7$ interfaces (V_{mod}=2 mV), and (right) corresponding point dI/dV spectra (positions marked in left panel; spectra are shifted vertically for clarity; point spectra taken from the same dI/dV map). **h**, dI/dV spectra along the line indicated in **c**. Scan parameters: **a**, V_{s}=-0.5 V, I_{t}=210 pA. **e**, V_{s}=-1.5 V, I_{t}=380 pA.

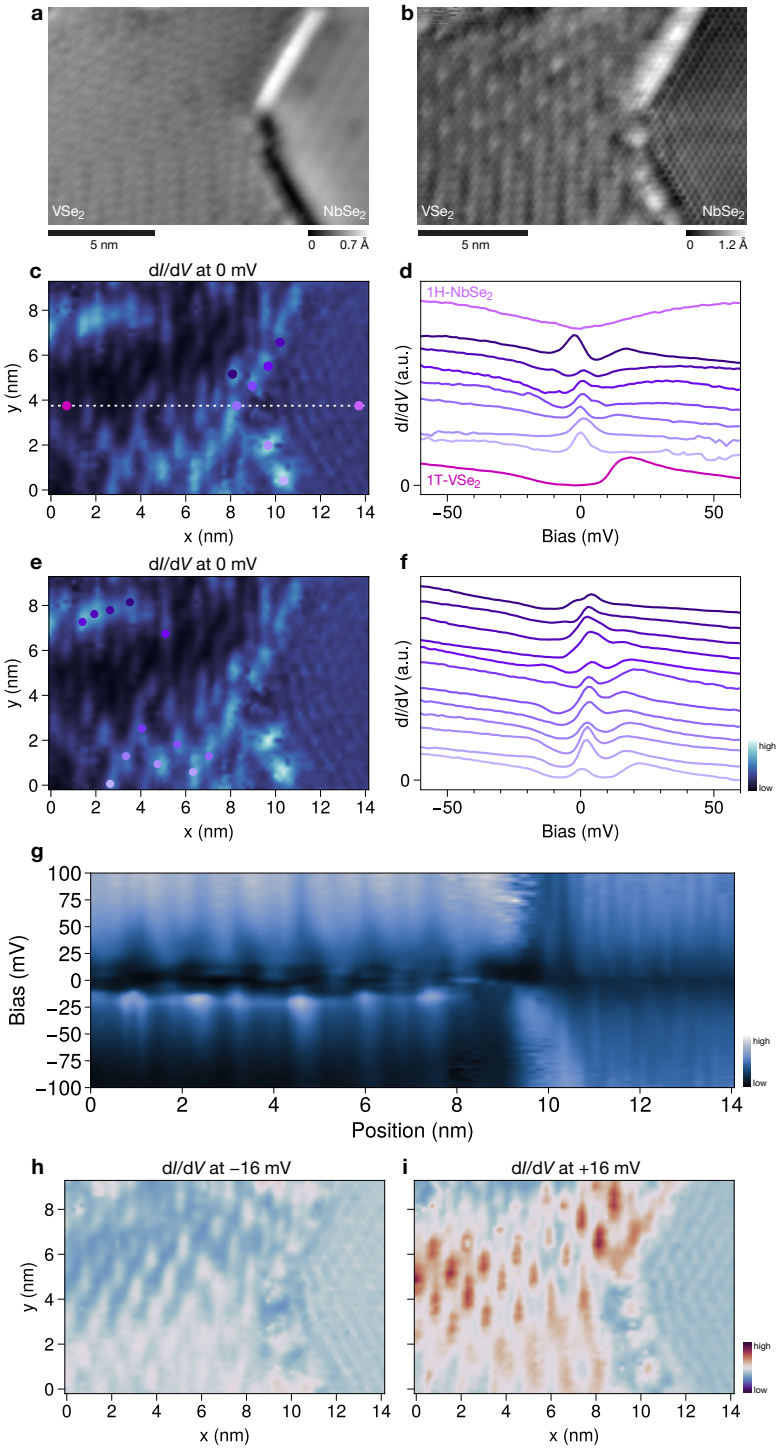

Fig. S12: Two lateral heterostructures and Kondo resonances in a side-coupled geometry. **a**, STM topography. V_s=+1.5 V, I_t=80 pA. **b**, STM topography with atomic resolution. V_s=−0.1 V, I_t= 79 pA. **c**, dI/dV map at 0 mV (V_{mod}=2 mV). **d**, dI/dV spectra of corresponding points in **c**, with points in 1T-VSe_2 and 1H-$NbSe_2$ (spectra are shifted vertically for clarity). **e**, dI/dV map at 0 mV (V_{mod}=2 mV) (same data as in panel c). Signatures of Kondo resonances can be found in VSe_2 up to ∼8 nm away from the interfaces. **f**, dI/dV spectra of corresponding points in **e** (spectra are shifted vertically for clarity). **g**, dI/dV spectra along the line indicated in **c**. **h** and **i**, Contrast inversion of a dI/dV map of these heterostructures at ±16 mV.

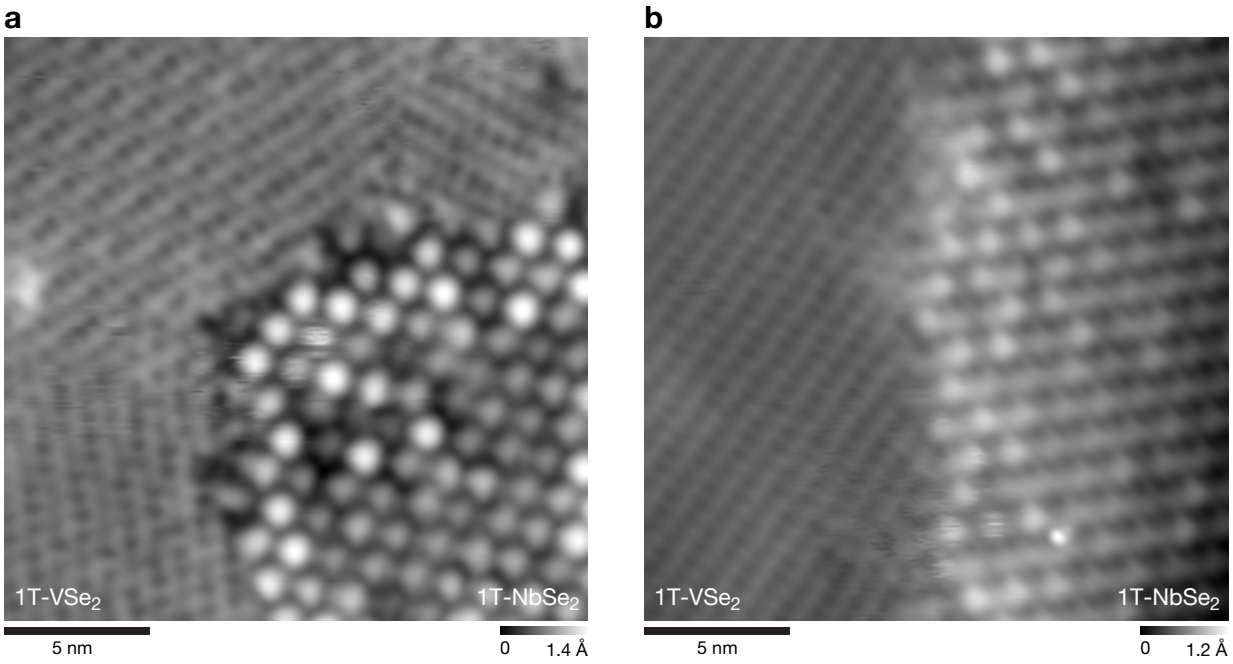

Fig. S13: Additional STM topography images of lateral heterostructures of 1T-VSe_2 and 1T-$NbSe_2$ islands. Also in this case neither CDW extends into the other material. Scan parameters: **a**, V_s=−0.247 V, I_t=62 pA. **b**, V_s=−1.5 V, I_t=150 pA.

DFT calculations

Electronic properties of 2D 1H-$NbSe_2$ and 1T-VSe_2

We tested the effect of the vdw-df2-b86r functional[S8] to the electronic properties of 2D 1H-$NbSe_2$ and 2D 1T-VSe_2. It is known that the vdw-df2-b86r functional with moderate U (e.g. 2 eV) is more appropriate to treat 1T-VSe_2[S9] as opposed to standard functionals such as PBE. Indeed, our DFT results in Figure S14 reveal that the vdw-df2-b86r gives minor quantitative changes in the 1T-VSe_2 band structure, specially at energies close to the Fermi level, while the band structure of 1H-$NbSe_2$ seems to be unaffected. Figure S15 shows the projected density of states (PDOS) and the simulated scanning tunneling spectroscopy (STS), both calculated with the vdw-df2-b86r and PBE functionals for comparison. Apart from very small shifts, the PDOS and simulated STS calculated with different functionals present overall the same phenomenology, specially the simulated STS, which is the most important aspect needed in this work. Thereby, we used the PBE functional with U = 2 eV throughout the calculations with the lateral interface.

Structural and electronic properties of the interfaces

Considering the PBE(U=2 eV) DFT setup defined in the previous section, we performed full relaxation and total energy calculations of different interface structures based on the edge scenarios I and II for the $NbSe_2$ island shown in Figure S16a. Given the nature of the edges in the $NbSe_2$ islands, the edges I and II can coexist in the same unit cell, for example, in the lateral heterostructure shown in Figure S16b, and four $NbSe_2/VSe_2$ interface candidates that can grow in registry were created based on the coordination number of either Nb or V atoms at the interface: I-$NbSe_6/VSe_5$, I-$NbSe_5/VSe_6$, II-$NbSe_6/VSe_7$ and II-$NbSe_7/VSe_6$ (Figures S16c-f, respectively). Notice that all four interfaces present the zig-zag pattern (top orange Se atoms) and parallel pattern (bottom yellow Se atoms) simultaneously. In order to investigate which interfaces in the lateral heterostructure are more energetically favorable

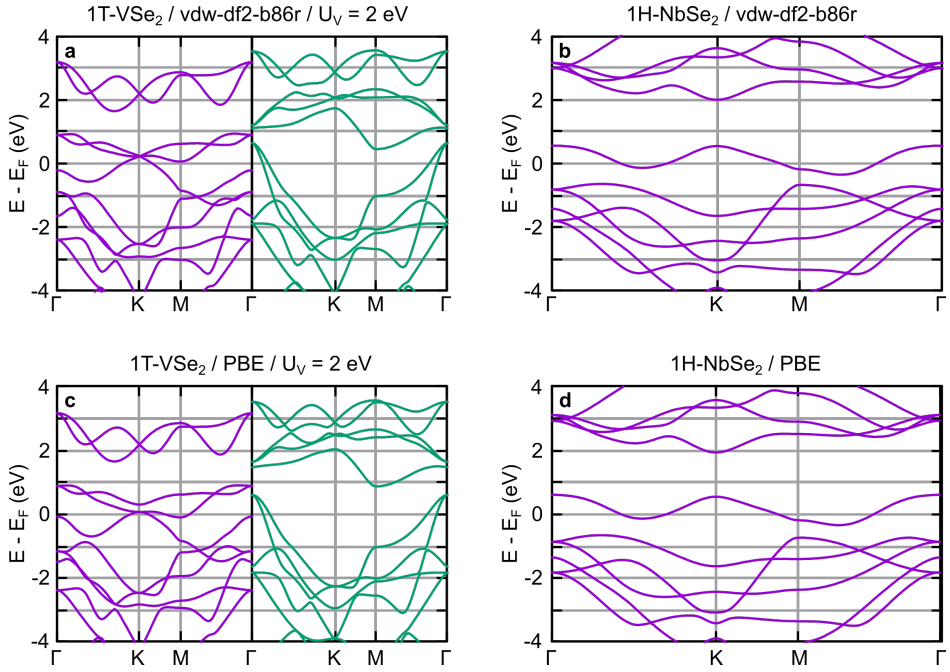

Fig. S14: DFT-calculated band structures of 2D 1H-$NbSe_2$ and 2D 1T-VSe_2 obtained with different functionals

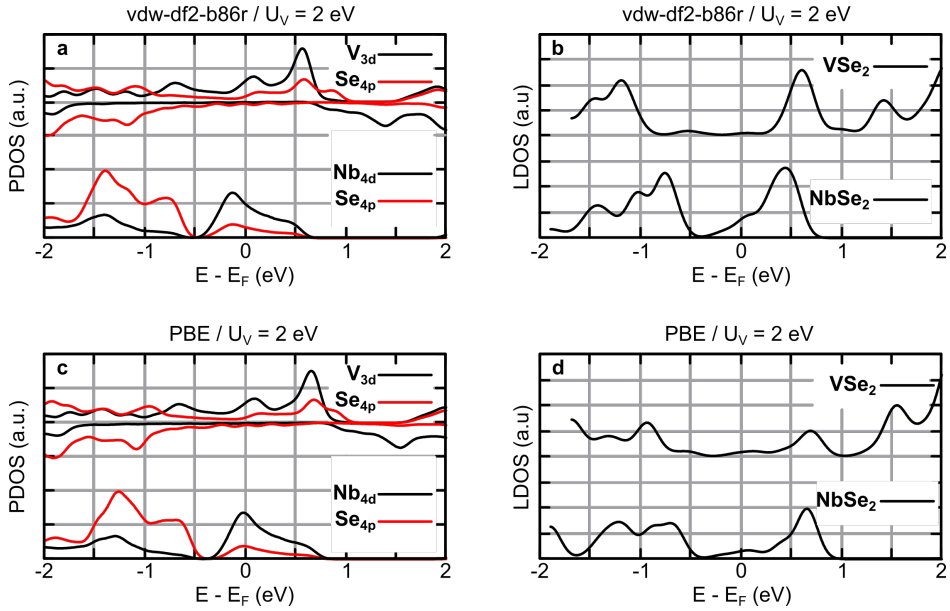

Fig. S15: DFT-calculated PDOS and simulated STS calculated by integrating the local density of states (LDOS) at a constant height of 3 Å over the topmost atom of each structure.

among the structures proposed here, we compared the total energy of structures that differ by only one of the interfaces, thus the total number of atoms will be the same. For example, by keeping the same type of interface I, we were able to calculate and compare the total

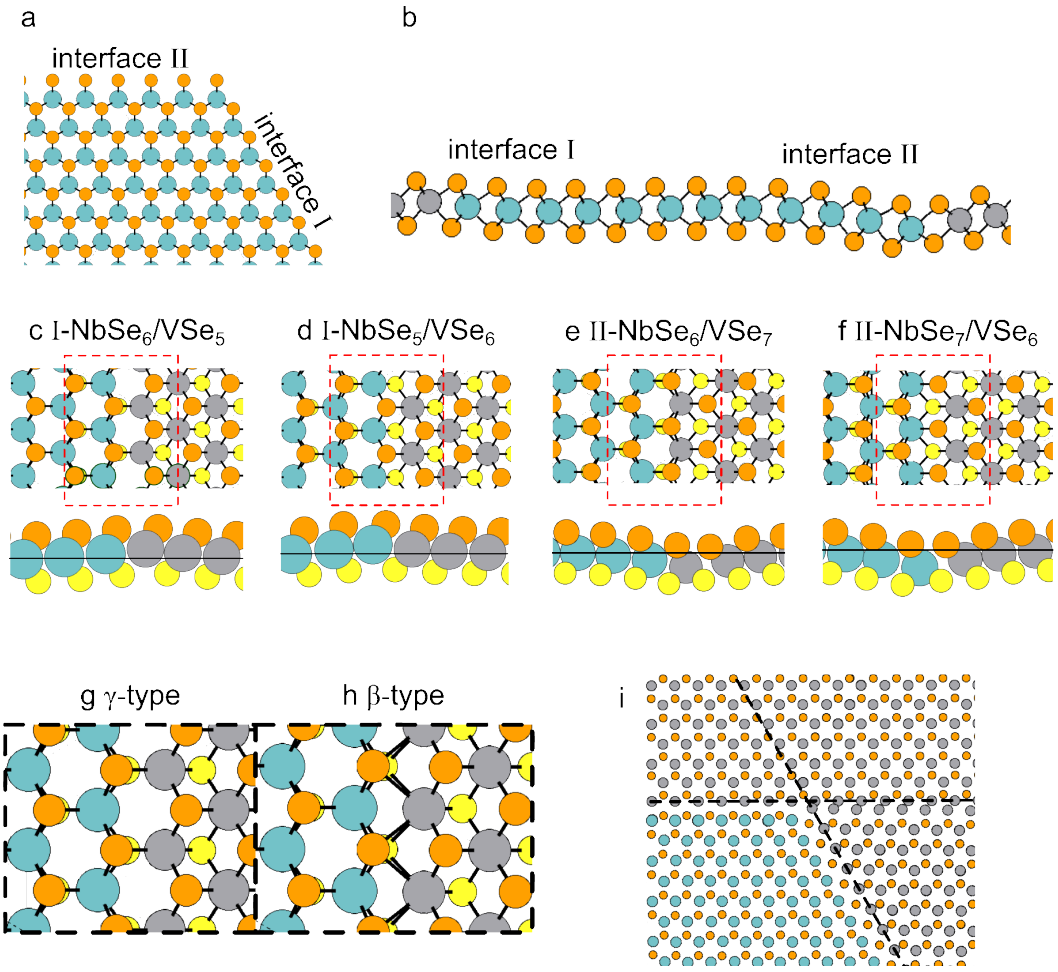

Fig. S16: a: top view of an $NbSe_2$ island showing two possible edge configurations. b: Side view of an example of lateral heterostructures. c-f: Proposed interfaces considered based on the coordination number of the Nb and V atoms at the lateral interface (A-side). g and h: Examples of the γ and β types of interfaces. i: Example of a tentative overlapping of a heterostructure with coexisting two β-type interface, showing that it cannot grow in registry (only Nb, V and top Se atoms are shown).

energies of the two types of interface II shown in Figure S16e and f, and the same procedure goes by keeping interface II as well. Our calculations show that among the type I interfaces, the I-$NbSe_6/VSe_5$ is more stable than the I-$NbSe_5/VSe_6$ by 0.2 eV, while among type II the II-$NbSe_7/VSe_6$ is more stable than II-$NbSe_6/VSe_7$ by 0.4 eV. Even though the total energies are affected by a twist of the unit cell that occurs in order to keep two interfaces, the energy spent in this deformation is two orders of magnitude smaller than the energy differences obtained here, thus not creating any artificial stability. We also stress that all interfaces

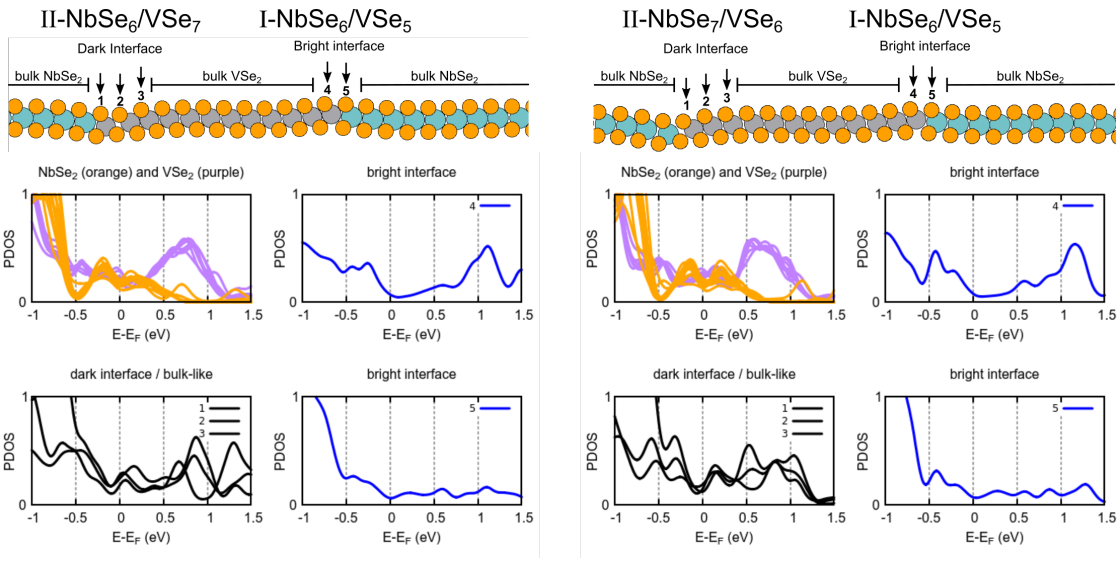

Fig. S17: DFT-calculated PDOS on the p_z orbitals of interface region Se atoms (A-side).

considered here are of the $\gamma-$type, whereas interfaces of the $\beta-$type do not grow in registry and would induce strong strain and reorganization of the interfaces, which is not compatible to the experimental results (see Figures S16g, h and i). Mixing of γ and β-types also cannot grow in registry. A simple way to distinguish the β- and γ-type interfaces is if transition metal atoms are aligned or not: for β-type, metal atoms are aligned in parallel, while for γ-type metal atoms are in a zigzag configuration at the interfaces.[S10]

The DFT-calculated energies indicate that the islands where the interfaces I-$NbSe_6/VSe_5$ and II-$NbSe_7/VSe_6$ coexist are preferable. However, even though the I-$NbSe_6/VSe_5$ is already expected to occur due to the stability of the edge I Nb having coordination six, it is very difficult to rule out the occurrence of the II-$NbSe_6/VSe_7$ interface just based on our STM and LDOS results. We then proceeded to investigate two lateral heterostructures shown in Figure S17, which differ only by the interface II. Additionally, the atomic contributions to the different STM signals and LDOS in the bright and dark interfaces are elucidated in more details in Figure S17, showing the DFT-calculated PDOS on the p_z orbitals of each top Se atom (A-side structure) of both lateral heterostructures. These are the atoms that contribute the most to the tunneling current, and will directly influence the contrast in the STM and LDOS either due to an electronic effect, for example having lower or higher density

of states, or due to the undulation of the relaxed structure. In both lateral heterostructures, the Se atom belonging to VSe_2 immediately at the bright interface has a significantly shifted PDOS compared to its surrounding Se atoms, which is then responsible to the strong bright features observed at -0.4 eV and 1.2 eV in the LDOS in the main text Figure 3f. Aside from a shift in energy, both features are consistent with the ones observed in the experiment at the bright interface. For the dark interface of the lateral heterostructure at the left of Figure S17, we observed a small attenuation of the PDOS of the Se at the interface belonging to the VSe_2, which are much lower in height than the other atoms in the bulk area. We then attribute in this case the darker contrast to both electronic and geometric effects. On the other hand, no attenuation is observed in the heterostructure at the right side of Figure S17, meaning that only the undulation is responsible to the dark contrast observed.

Figure S18 shows the alternative lateral heterostructure where only interface II is different from the one presented in the main text. The simulated STM images for the two types of interface II structures (VSe_7—$NbSe_6$ / VSe_6—$NbSe_7$) are quite similar but as mentioned before VSe_7—$NbSe_6$ was found to be less stable based on DFT.

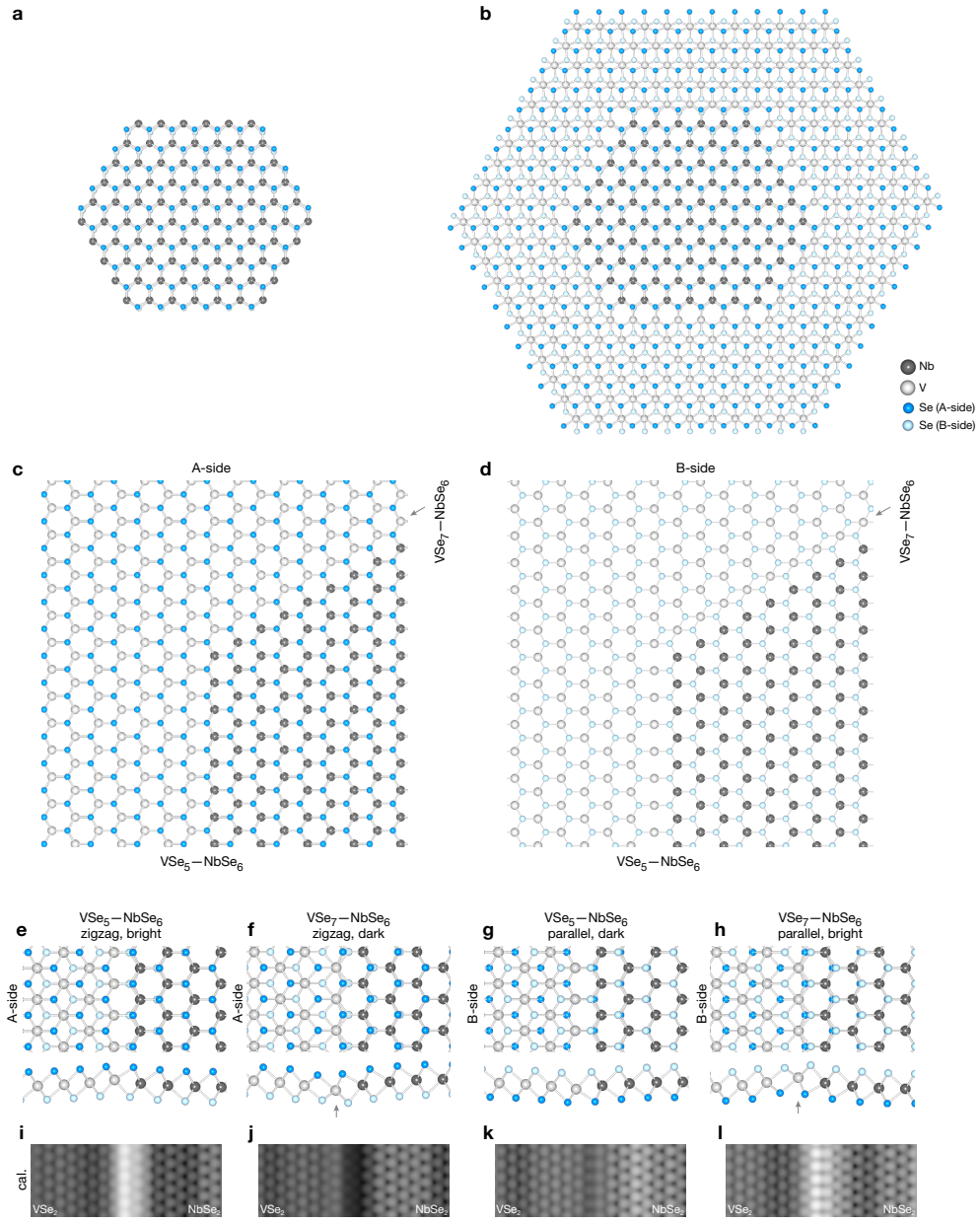

Fig. S18: Alternative lateral heterostructure geometry with VSe_5—$NbSe_6$ and VSe_7—$NbSe_6$ interfaces. Compared to results reported in main text, the structure of the VSe_5—$NbSe_6$ interface remains unaltered. The main structural difference between VSe_7—$NbSe_6$ and VSe_6—$NbSe_7$ is that a line of transition metal atoms at the interface is replaced from V atoms to Nb atoms (indicated by the grey arrows in panels **c**, **d**, **f** and **h**). DFT calculations suggest VSe_6—$NbSe_7$ is more stable. **a**, **b**, Schematics of the formation of a lateral heterostructure in this geometry: VSe_2 and $NbSe_2$ can also grow in-registry with VSe_5—$NbSe_6$ and VSe_7—$NbSe_6$ interfaces. **c**, **d**, Zoom-in schematic of two interfaces with views from A-side (with A-side Se atoms only) and B-side (with B-side Se atoms only), respectively. Grey arrows indicate the difference between VSe_7—$NbSe_6$ and VSe_6—$NbSe_7$ (schematic structures without relaxation). **e**–**h**, Top view and side view of the these lateral heterostructures of VSe_5—$NbSe_6$ and VSe_7—$NbSe_6$, and **i**–**l**, their corresponding calculated STM images (V_s=−0.5 V) (calculated structures with relaxation). Grey arrows indicate the difference between VSe_7—$NbSe_6$ and VSe_6—$NbSe_7$.

References

(S1) Liu, Z.-L.; Wu, X.; Shao, Y.; Qi, J.; Cao, Y.; Huang, L.; Liu, C.; Wang, J.-O.; Zheng, Q.; Zhu, Z.-L.; Ibrahim, K.; Wang, Y.-L.; Gao, H.-J. Epitaxially Grown Monolayer VSe_2 : An Air-Stable Magnetic Two-Dimensional Material with Low Work Function at Edges. *Science Bulletin* **2018**, *63*, 419–425.

(S2) Akber, H.; Shan, H.; Mao, Y.; Yao, J.; Zhai, X.; Zhao, A. Nonreciprocal Charge-Density-Wave Proximity Effect in a Lateral Heterojunction of $NbSe_2/TiSe_2$. *Appl. Phys. Lett.* **2024**, *124*, 071602.

(S3) Zhang, Q.; Fan, J.; Zhang, T.; Wang, J.; Hao, X.; Xie, Y.-M.; Huang, Z.; Chen, Y.; Liu, M.; Jia, L.; Yang, H.; Liu, L.; Huang, H.; Zhang, Y.; Duan, W.; Wang, Y. Visualization of Edge-Modulated Charge-Density-Wave Orders in Monolayer Transition-Metal-Dichalcogenide Metal. *Commun. Phys.* **2022**, *5*, 117.

(S4) Lozovoy, K. A.; Dirko, V. V.; Kukenov, O. I.; Sokolov, A. S.; Krukovskii, K. V.; Snegerev, M. S.; Borisov, A. V.; Kistenev, Y. V.; Kokhanenko, A. P. RHEED Study of the Epitaxial Growth of Silicon and Germanium on Highly Oriented Pyrolytic Graphite. *C* **2024**, *10*, 36.

(S5) Soumyanarayanan, A.; Yee, M. M.; He, Y.; van Wezel, J.; Rahn, D. J.; Rossnagel, K.; Hudson, E. W.; Norman, M. R.; Hoffman, J. E. Quantum Phase Transition from Triangular to Stripe Charge Order in $NbSe_2$. *Proc. Natl. Acad. Sci* **2013**, *110*, 1623–1627.

(S6) Flicker, F.; van Wezel, J. Charge Ordering Geometries in Uniaxially Strained $NbSe_2$. *Phys. Rev. B* **2015**, *92*, 201103.

(S7) Cossu, F.; Palotás, K.; Sarkar, S.; Di Marco, I.; Akbari, A. Strain-Induced Stripe Phase in Charge-Ordered Single Layer $NbSe_2$. *NPG Asia Mater.* **2020**, *12*, 24.

(S8) Hamada, I. van der Waals Density Functional Made Accurate. *Phys. Rev. B* **2014**, *89*, 121103.

(S9) Kezilebieke, S.; Huda, M. N.; Dreher, P.; Manninen, I.; Zhou, Y.; Sainio, J.; Mansell, R.; Ugeda, M. M.; van Dijken, S.; Komsa, H.-P.; Liljeroth, P. Electronic and Magnetic Characterization of Epitaxial VSe_2 Monolayers on Superconducting $NbSe_2$. *Commun. Phys.* **2020**, *3*, 116.

(S10) Lin, Y. C.; Dumcenco, D. O.; Huang, Y. S.; Suenaga, K. Atomic Mechanism of the Semiconducting-to-Metallic Phase Transition in Single-Layered MoS_2. *Nat. Nanotechnol.* **2014**, *9*, 391–396.